

UNCERTAINTY QUANTIFICATION IN MD SIMULATIONS. PART II: BAYESIAN INFERENCE OF FORCE-FIELD PARAMETERS*

F. RIZZI[†], H. N. NAJM[‡], B. J. DEBUSSCHERE[‡], K. SARGSYAN[‡], M. SALLOUM[‡],
H. ADALSTEINSSON[‡], AND O. M. KNIO[§]

Abstract. This paper explores the inference of small-scale, atomistic parameters, based on the specification of large, or macroscale, observables. Specifically, we focus on estimating a set of force-field parameters for the four-site, TIP4P, water model, based on a synthetic problem involving isothermal, isobaric molecular dynamics (MD) simulations of water at ambient conditions. We exploit the polynomial chaos (PC) expansions developed in Part I as surrogate representations of three macroscale observables, namely density, self-diffusion, and enthalpy, as a function of the force-field parameters. We analyze and discuss the use of two different PC representations in a Bayesian framework for the inference of atomistic parameters, based on synthetic observations of three macroscale observables. The first surrogate is a *deterministic* PC representation, constructed in Part I using nonintrusive spectral projection (NISP). An alternative strategy exploits a *nondeterministic* PC representation obtained using Bayesian inference of PC coefficients. We analyze the sensitivity of selected force-field parameters to the macroscale data, namely by exploiting the surrogate models to derive suitable “response” surfaces in the space of random parameters. The performance of both inference strategies is then examined in light of this analysis. The results show that each parameter is very sensitive to certain observables, while being only minimally affected by others. We show that a suitable choice of the observables allows us to recover the presumed “true” set of parameters with high accuracy even with low-order surrogate models.

Key words. uncertainty quantification, inverse problem, Bayesian inference, polynomial chaos, molecular dynamics, TIP4P water, surrogate model

AMS subject classifications. 60G15, 62F15, 82D15, 62C10, 65C40, 74F05, 82C05, 82C22

DOI. 10.1137/110853170

1. Introduction. Numerous models have been developed in the past to provide suitable descriptions of the properties of water, particularly by developing appropriate governing potentials (see, e.g., [14, 8, 13, 35, 34, 33] and the references therein). A popular approach has been to employ an empirical force-field description, in which pairwise-additive functions are fitted to reproduce bulk-phase experimental data in classical Monte Carlo or molecular dynamics (MD) simulations. Examples of this class include RWK [26], SPC/E [4], TIP4P [12], TIP4P-Ew [10], and TIP5P [18] representations. These force-field representations are often capable of reproducing some physical properties of water with a good degree of accuracy.

In this work, we explore the use of Bayesian inference to estimate force-field

*Received by the editors October 27, 2011; accepted for publication (in revised form) August 21, 2012; published electronically December 12, 2012. This research was supported by the U.S. Department of Energy, Office of Advanced Scientific Computing Research, under award DE-SC0002506. Sandia National Laboratories is a multiprogram laboratory managed and operated by Sandia Corporation, a wholly owned subsidiary of Lockheed Martin Corporation, for the U.S. Department of Energy’s National Nuclear Security Administration under contract DE-AC04-94AL85000.

[†]<http://www.siam.org/journals/mms/10-4/85317.html>

[‡]Department of Mechanical Engineering, Johns Hopkins University, Baltimore, MD 21218 (frizzil@jhu.edu).

[§]Sandia National Laboratories, Livermore, CA 94550 (hnajm@sandia.gov, bjdebus@sandia.gov, ksargsy@sandia.gov, mnsallo@sandia.gov, hadalst@sandia.gov).

[§]Corresponding author. Department of Mechanical Engineering, Johns Hopkins University, Baltimore, MD 21218. Current address: Department of Mechanical Engineering and Materials Science, Duke University, Durham, NC 27708 (omar.knio@duke.edu).

parameters of the four-site (or TIP4P) model using bulk-phase properties of water. The emphasis is on the possibility of estimating *atomistic* model parameters using a set of *macroscale* observables. The Bayesian approach provides a framework for tackling this problem, which involves both “noisy” data and parametric uncertainties. Previous work employing Bayesian inference for calibration of force fields was conducted by Cailliez and Pernot [5], who focused on calibrating the Lennard-Jones (LJ) parameters for Argon using experimental-based data for vapor viscosity and the second virial coefficient. The authors relied on Markov chain Monte Carlo (MCMC) methods to sample the parameter space. In this case, this strategy was cost-effective because of the availability of analytical expressions relating the observables to the LJ parameters. In general, however, when analytical expressions are not available and the evaluation of a forward problem for a given parameter set is computationally intensive, the problem can become prohibitively expensive.

To overcome this issue, a number of alternatives have been proposed. Efendiev, Hou, and Luo [6] introduced a preconditioning of MCMC methods using coarse-scale models aimed at reducing the fine-scale computational cost and increasing the acceptance rate in the MCMC sampling. Wang and Zabaras [36] exploited proper orthogonal decomposition (POD) to construct a reduced-order model for the direct simulations in a radiative heat-source inverse problem. Ma and Zabaras [17] introduced an adaptive hierarchical sparse grid collocation method to construct an interpolant to the forward model solution, which was then used as a stochastic surrogate model for calculating the likelihood. Gaussian processes (GPs) have also been used as surrogates to approximate the output of complex computational models; see, e.g., [24, 15, 21, 22, 23, 25, 3]. Formally, a GP is a stochastic process generating samples over a time or spatial domain such that any finite subset of samples follows a multivariate Gaussian distribution. GPs are completely defined by a mean and covariance structure and can be interpreted as extensions of multivariate Gaussian distributions to infinite dimensionality. A key feature for constructing a GP surrogate is the selection of a suitable kernel function, such that samples drawn from the resulting GP representation suitably approximate the output of the targeted complex model. In general, the construction of a suitable GP surrogate can be obtained as a two-stage procedure. In the first stage, generally referred to as “calibration,” a set of runs of the targeted complex model is exploited as training data to define the structure of the surrogate. In the second stage, referred to as “validation,” the GP surrogate is validated by comparing its predictions against new runs of the complex model at locations different from those in the training data; see, e.g., [25, 3]. The quality of the GP representation may be limited by two main factors [3]: first, the assumption of a stationary GP may be not be suitable, and, second, a poor choice of the training data set may lead to poor representations, especially when little information is available about the model behavior.

Marzouk, Najm, and Rahn [19] developed a surrogate model approach where a spectral reformulation of the forward problem is used to determine a polynomial chaos (PC) expansion response surface, which is then exploited as a surrogate to avoid costly forward model evaluations. The method introduced in [19] can be readily used for the purposes of the present work. In Part I [28], we applied a stochastic reformulation of the forward MD system of TIP4P water at ambient conditions, $T = 298$ K and $P = 1$ atm, and constructed the PC expansions of three macroscale observables: density, self-diffusivity, and enthalpy. Following [19], we can use these PC representations as a surrogate model to efficiently formulate the inverse problem under consideration. For demonstration purposes, we focus on a synthetic problem where test values of

the TIP4P parameters are used to generate a collection of noisy data of density, self-diffusion, and enthalpy. These data are then used in conjunction with the PC surrogates to infer back the “true” force-field parameters.

The use of Bayesian inference in the fashion outlined above is not, in itself, new. In particular, the present methodology is similar to that used in [19], which also focused on synthetic tests based on postulated “true” model parameters and considered noisy data in a diffusion-based source inversion problem. In the present work, however, distinctive features arise due to the fact that the problem under consideration originates within an MD context. In fact, intrinsic (or sampling) “noise,” which is inherently present in atomistic systems due to thermal fluctuations of the atoms, is an important source of uncertainty. Small systems tend to have large instantaneous fluctuations, and controlling the noise level just by averaging over multiple realizations of the system is a prohibitive approach for most applications, due to the large computational cost associated with atomistic simulations. As discussed in [28], the effect of the intrinsic “noise” may lead to *uncertain* PC surrogates, i.e., PC representations whose coefficients themselves are random variables (RVs). It follows that a suitable inference formulation should be developed to account for this additional source of uncertainty. We adopt a synthetic test case rather than resorting to experimental data, mainly to avoid addressing additional challenges due to independence, biases, and correlation. The main goal of this work is not to reparametrize the TIP4P water model, i.e., to redefine its main parameters, for which experimental data would be necessary, but rather to explore, in this regard, the potential of using a Bayesian inference approach. In particular, we aim at exploring what the implications are of choosing a particular observable in an MD setting, quantifying the information gain in the parameters when a specific observable is chosen over another and, also, characterizing the dependence of the inference results on the order and type of surrogate model. The synthetic application provides a suitable setting for investigating these questions, which we regard as a necessary basis in anticipation of a future study targeting the refinement of the water model parameters based on experimental data.

We present two separate formulations of the inverse problem according to the type of PC expansion chosen as the surrogate model. We first discuss the formulation of the inverse problem based on a PC surrogate obtained using nonintrusive spectral projection (NISP) [28]. In this case, the PC representations are *deterministic* expansions where each PC coefficient has a single, well-defined value. In situations where the intrinsic noise in the MD-based observables is large, due, e.g., to small MD systems, it may be more appropriate to infer the PC surrogate with Bayesian inference [28]. In this case, the PC expansions are *nondeterministic* because their coefficients are RVs defined by a specific joint probability density. Previous work with an uncertain forward model has been done in the context of stochastic reaction networks in [31]. The uncertainty in the coefficients provides an important source of information that may have relevant impact on the inference results. To this end, we illustrate a formulation that allows us to properly account for this uncertainty. We show that both approaches can be suitably employed to recover the “true” force-field parameters with high accuracy using low-order surrogate models.

This article is organized as follows. In section 2, we introduce the inverse problem under study and illustrate the mathematical formulation based on *deterministic* (section 2.4.1) and *nondeterministic* (section 2.4.2) surrogate models. In section 3, we present and discuss the results, while a summary and conclusions are addressed in section 4.

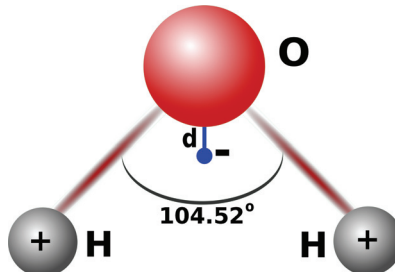


FIG. 2.1. Structure of the four-site, TIP4P model of water. H and O are the hydrogen and oxygen atoms, respectively, the + and - signs represent the charges, and d is the distance from the oxygen to the massless negative charge.

2. Theoretical background and formulation. The inverse problem under consideration involves the inference of force-field parameters for the TIP4P water model given a set of observations of one or more macroscale observables of water. The TIP4P model is also referred to as a four-site model, due to the fact that the negative charge of the oxygen atoms is placed on a massless site at a distance d from the oxygen along the bisector of the HOH angle; see Figure 2.1. We focus on a synthetic problem where fixed values of the TIP4P force-field parameters are used to run isothermal, isobaric MD simulations at ambient conditions, $T = 298$ K and $P = 1$ atm, and collect a set of noisy data of selected macroscale observables. The MD computational setting is the one introduced in Part I [28]. This data is then exploited in a Bayesian setting to recover the “true” set of driving parameters. For the purposes of the present work, we limit our attention to inferring three parameters, ε , σ , and d . The first two, ε and σ , define the shape of LJ potential,

$$(2.1) \quad V_{LJ} = 4\varepsilon \left\{ \left(\frac{\sigma}{r} \right)^{12} - \left(\frac{\sigma}{r} \right)^6 \right\},$$

where V_{LJ} is the induced potential, ε represents the depth of the potential well, σ is the distance at which the potential becomes zero, and r is the distance between two particles. The LJ potential describes repulsion and dispersion interactions and is one of two components, the other being a Coulombic interaction, defining the intermolecular potential for TIP4P water; see Part I [28] for the details of the MD setting. The other parameter under consideration, d , identifies the distance from the oxygen atom to the massless point where the negative charge is placed in the TIP4P geometry; see Figure 2.1.

The analysis can be regarded as a three-stage process: first, three values of the parameters of interest, $\varepsilon = \hat{\varepsilon}$, $\sigma = \hat{\sigma}$, and $d = \hat{d}$, are chosen and regarded as the “true” parameters (the “hat” will be used below to denote the “true” values); second, these “true” values are used to run N replica MD simulations and obtain, exploiting the time-averaging methods discussed in section 2 of [28], N realizations of density, self-diffusion, and enthalpy; finally, these $3N$ observations are used within a Bayesian inference framework to recover the original (or “true”) subset of driving parameters. As mentioned in the introduction, our goals are two-fold: (i) to explore the implications resulting from choosing particular macroscale observables in the present MD setting; and (ii) to investigate the performance of the Bayesian approach in terms of the accuracy with which we recover the “true” parameters and characterize the main factors affecting the inference.

2.1. Collection of observations. To collect the observations for the macroscale observables of interest, density (ρ), self-diffusion (D), and enthalpy (H), we proceed as follows. To fix the force-field parameters, we choose the following values:

$$(2.2) \quad \begin{aligned} \hat{\varepsilon} &= 0.17, \text{ kcal/mol}, \\ \hat{\sigma} &= 3.15, \text{ \AA}, \\ \hat{d} &= 0.14, \text{ \AA}, \end{aligned}$$

and we set the remaining parameters equal to their values commonly used in computational applications of TIP4P water [12, 11]. By initializing the velocity field of the atoms using $N = 10$ different ensembles drawn from a distribution consistent with the desired temperature ($T = 298$ K) of the system, we create and run 10 replica MD simulations. The number (10) of runs is purposely chosen to mimic the situation when only a limited number of data points is available.

We then apply the time-averaging methods described in section 2 of [28] to collect N realizations for each observable of interest, i.e., ρ , D , and H . This approach allows us to exploit the inherent variability of the MD setting to obtain noisy synthetic data, and, thus, there is no need to define a particular noise model to mimic experimental data.

For simplicity, denoting $G_1 \equiv \rho$, $G_2 \equiv D$, and $G_3 \equiv H$, the observations can be written in short form as

$$(2.3) \quad \mathbf{G}_k = \{G_k^i\}_{i=1}^N, \quad k = 1, 2, 3,$$

where G_k^i represents the i th observation obtained for the k th observable, and $N = 10$. Figure 2.2 shows the data sets $\{G_k^i\}_{i=1}^{10}$, $k = 1, 2, 3$, obtained using the “true” parameter values defined in (2.2). To evaluate the strength of the noise, we estimate the coefficient of variation for each set, obtaining 0.001346 for density, 0.055010 for self-diffusion, and 0.000885 for enthalpy. Consistent with the discussion in Part I, this shows that in the present case the noise level is small.

2.2. Inverse problem formulation. In general, a convenient approach to inverse problems relies on a *direct* Bayesian framework which, for the problem under consideration, can be formulated as follows. Consider a set of N observations, $\mathbf{G}_k = \{G_k^i\}_{i=1}^N$, for each quantity of interest (QoI), G_k , $k = 1, 2, 3$, and a prediction, $\mathcal{F}_k(\varepsilon, \sigma, d)$, for the k th observable obtained by running a *full* MD simulation for a given set of parameters (ε, σ, d) . We can use Bayes’s theorem [32] to define a posterior probability density for (ε, σ, d) , given the data sets \mathbf{G}_k , $k = 1, 2, 3$, according to

$$(2.4) \quad \pi(\varepsilon, \sigma, d | \{\mathbf{G}_k\}_{k=1}^3) = \frac{p(\{\mathbf{G}_k\}_{k=1}^3 | \varepsilon, \sigma, d) q(\varepsilon, \sigma, d)}{C},$$

where $\pi(\varepsilon, \sigma, d | \{\mathbf{G}_k\}_{k=1}^3)$ is the posterior density, $p(\{\mathbf{G}_k\}_{k=1}^3 | \varepsilon, \sigma, d)$ is the likelihood, $q(\varepsilon, \sigma, d)$ is the prior on the parameters, and C is a normalization constant. The observations, $\{\mathbf{G}_k\}_{k=1}^3$, appear in the formulation above only through the likelihood, $p(\{\mathbf{G}_k\}_{k=1}^3 | \varepsilon, \sigma, d)$, which can be interpreted as a function of the parameters, i.e., $\mathcal{L}(\{\varepsilon, \sigma, d\}; \{\mathbf{G}_k\}_{k=1}^3) = p(\{\mathbf{G}_k\}_{k=1}^3 | \varepsilon, \sigma, d)$.

A suitable likelihood function can be formulated assuming that independent additive errors account for the deviation between predicted, $\mathcal{F}_k(\varepsilon, \sigma, d)$, $k = 1, 2, 3$, and observed, $\{G_k^i\}_{i=1}^N$, $k = 1, 2, 3$, values according to

$$(2.5) \quad G_k^i = \mathcal{F}_k(\varepsilon, \sigma, d) + \gamma_k^i, \quad k = 1, 2, 3, \quad i = 1, \dots, N,$$

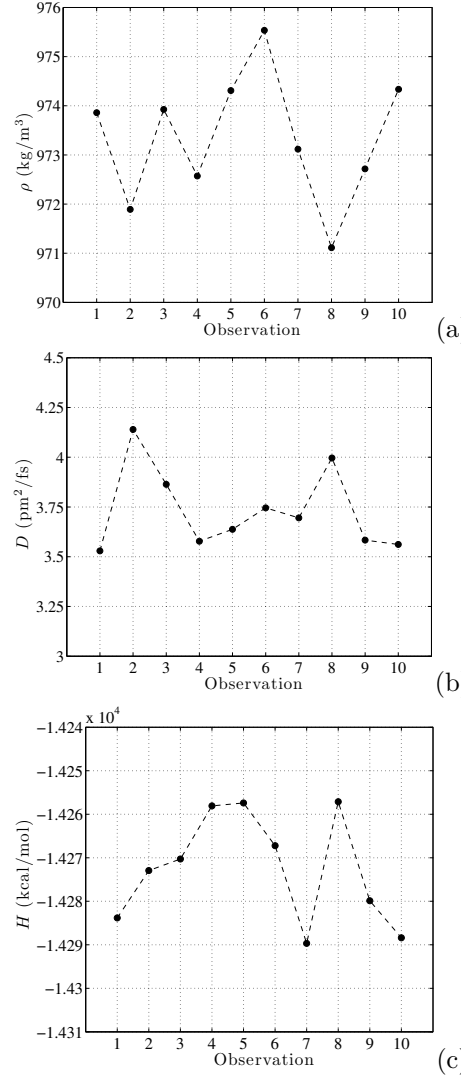


FIG. 2.2. Data sets, $\mathbf{G}_k = \{G_k^i\}_{i=1}^{10}$, obtained for (a) density, (b) self-diffusivity, and (c) enthalpy collected from 10 independent replica simulations of the MD system based on the “true” force-field parameters (2.2).

where each set $\{\gamma_k^i\}_{i=1}^N$, $k = 1, 2, 3$, comprises independent and identically distributed (i.i.d.) RVs with corresponding density p_{γ_k} , $k = 1, 2, 3$. Assuming $\gamma_k^i \sim \mathcal{N}(0, \tilde{\sigma}_k^2)$, $i = 1, \dots, N$, $k = 1, 2, 3$, with $\tilde{\sigma}_k^2$ being the variance, and considering N independent realizations for each observable, the likelihood function is expressed as

$$(2.6) \quad \mathcal{L}(\{\varepsilon, \sigma, d\}; \mathbf{G}_1, \mathbf{G}_2, \mathbf{G}_3) = \prod_{k=1}^3 \prod_{i=1}^N p_{\gamma_k} (G_k^i - \mathcal{F}_k(\varepsilon, \sigma, d)).$$

The above formulation reflects two main assumptions. First, we assume the three observables to be independent, which leads to the factorization with the k -index. This has been verified for the present case by performing a large set of MD runs and showing

not only that the joint density between each pair of observables closely resembles a Gaussian but also that the observables have weak or nearly absent correlations. This result justifies the independence assumption in the present case, but, for brevity, we omit the details and refer the reader to [27]. Second, for a given observable, assuming independence between the corresponding N data points shown in Figure 2.2 is a valid hypothesis, due to the fact that these observations are obtained from N independent replica simulations of the nominal MD system. In a computational setting, MCMC methods for solving Bayes's formula require a large number of evaluations of the likelihood function (2.6), each of which requires a *full* MD simulation, for a given set (ε, σ, d) , to obtain the corresponding prediction $\mathcal{F}_k(\varepsilon, \sigma, d)$. It follows that this *direct* Bayesian approach quickly becomes prohibitive in the present context, due to the large computational cost associated with a single MD computation. Computationally intensive forward problems thus pose a serious limitation, and the direct method illustrated above becomes unfeasible for most practical applications of interest. To address this issue, a number of strategies have been proposed in the past, including GP surrogates [15], preconditioning of MCMC methods [6], using POD to construct a reduced-order model of the direct simulations [36], and the use of an adaptive hierarchical sparse grid collocation method to build an interpolant to the solution of the forward model, which is then used as a surrogate [17].

In the present study, we follow the approach developed in [19], which involves two key stages: first, PC expansions of selected QoIs are built using a stochastic spectral reformulation of the forward problem; second, these PC representations are used as surrogates to replace the full forward problem prediction. The first step listed above has been implemented in Part I [28]. Below, we briefly recall the main features of the stochastic reformulation of the forward MD problem.

2.3. Surrogate model and review of Part I. In Part I, a stochastic reformulation of the forward problem was introduced assuming three force-field parameters to be nondeterministic; see section 3 of [28]. In particular, we considered uncertain the two LJ parameters ε and σ and the distance, d , from the oxygen atom to the massless point where the negative charge is placed in the TIP4P model. The uncertainty was expressed according to

$$(2.7) \quad \begin{aligned} \varepsilon(\xi_1) &= 0.147 + 0.043 \xi_1, & \text{kcal/mol}, \\ \sigma(\xi_2) &= 3.15061 + 0.021 \xi_2, & \text{\AA}, \\ d(\xi_3) &= 0.14 + 0.035 \xi_3, & \text{\AA}, \end{aligned}$$

where $\{\xi_i\}_{i=1}^3$ are i.i.d. standard RVs uniformly distributed over the interval $(-1, 1)$, i.e., $\{\xi_i\}_{i=1}^3 \sim \mathcal{U}(-1, 1)$ (see [28] for the details about nominal values and ranges of the above expansions). For later convenience, we denote $\boldsymbol{\theta} = \{\varepsilon, \sigma, d\}$ and recast the above reformulation in the following simplified form:

$$(2.8) \quad \boldsymbol{\theta} = \mathbf{f}(\boldsymbol{\xi}).$$

Since the model parameters are uncertain, the MD predictions are also uncertain and were thus represented in terms of PC expansions [37, 7, 16]. We limited our attention to three QoIs, namely density, ρ , self-diffusivity, D , and enthalpy, H , and represented them using Wiener-Legendre (WLe) expansions according to

$$(2.9) \quad \{\rho, D, H\} \approx M_k(\boldsymbol{\xi}) = \sum_{l=0}^P c_l^{(k)} \Psi_l(\boldsymbol{\xi}), \quad k = 1, 2, 3,$$

where $\{c_l^{(k)}\}_{l=0}^P$ is the set of PC coefficients for the k th observable, $\Psi_l(\boldsymbol{\xi})$ is the l th multidimensional Legendre polynomial with an argument in the three-dimensional (3D) space $(-1, 1)^3$, $P = (3 + p)!/3!/p! - 1$, and p is the degree of the polynomial expansion.

To compute the PC coefficients, we followed two different approaches: NISP and Bayesian inference. Due to the low dimensionality of the problem, NISP was applied using a fully tensorized Gauss quadrature. This approach could be suitably implemented because the noise level was small enough to be controlled through averaging. As an alternative to NISP, the Bayesian approach was used, which is particularly suitable for cases when the former becomes unfeasible. Limitations to NISP arise in a high-dimensional setting in which one may not be able to sample sufficiently to adequately control quadrature errors and cases where the MD model output cannot be averaged sufficiently to ensure negligible noise.

Regardless of the relative merits of these two approaches, it is important to highlight a key feature distinguishing the corresponding PC representations. Specifically, the NISP approach yields PC representations with *deterministic* coefficients, whereas Bayesian inference yields PC expansions with *nondeterministic* coefficients, i.e., RVs characterized by a joint probability distribution. This consideration suggests that different formulations of the inverse problem are needed according to the type of PC representation chosen as surrogate model, as further discussed below.

2.4. Mathematical formulation.

2.4.1. Deterministic surrogate model. In this subsection, we formulate the inverse problem using as the surrogate model for the observables of interest the *deterministic* PC expansions obtained in Part I with the NISP approach.

Recalling that ξ_1 , ξ_2 , and ξ_3 are i.i.d. uniform RVs over the interval $(-1, 1)$, drawing samples $\boldsymbol{\xi}^{(j)}$ from their distributions yields, according to (2.7), samples of the force-field parameters $\boldsymbol{\theta}^{(j)} = \mathbf{f}(\boldsymbol{\xi}^{(j)})$, namely $\varepsilon(\xi_1^{(j)})$, $\sigma(\xi_2^{(j)})$, and $d(\xi_3^{(j)})$. The same sample, $\boldsymbol{\xi}^{(j)}$, can be used to evaluate the PC expansions (2.9) according to

$$(2.10) \quad M_k(\boldsymbol{\xi}^{(j)}) = \sum_{l=0}^P c_l^{(k)} \Psi_l(\boldsymbol{\xi}^{(j)}) , \quad k = 1, 2, 3,$$

where, in this case, $\{c_l^{(k)}\}_{l=0}^P$ are the NISP-based *deterministic* PC coefficients. Consequently, (2.10) represents the prediction of the k th observable obtained by evaluating the NISP-based surrogate model of order p , and it corresponds to a specific realization $\mathbf{f}(\boldsymbol{\xi}^{(j)})$ of the parameters. Replacing the *full* MD prediction \mathcal{F}_k in (2.5) and (2.6) with the surrogate model prediction, M_k , yields a likelihood function that depends explicitly on $\boldsymbol{\xi}$ according to

$$(2.11) \quad \mathcal{L}(\{\xi_1, \xi_2, \xi_3\}; \mathbf{G}_1, \mathbf{G}_2, \mathbf{G}_3) = \prod_{k=1}^3 \prod_{i=1}^N p_{\gamma_k} (G_k^i - M_k(\xi_1, \xi_2, \xi_3)) ,$$

where the index k enumerates the observables and i enumerates the observations. This reformulation implies that we are implicitly assuming $G_k^i = M_k(\boldsymbol{\xi}) + \gamma_k^i$, $k = 1, 2, 3$, $i = 1, \dots, N$; i.e., γ_k^i represents the discrepancy between the i th observation, G_k^i , of the k th observable and the corresponding *surrogate* model prediction, $M_k(\boldsymbol{\xi})$. In this case, holding the zero mean noise assumption reflects our assertion that there is no bias in the model predictions with respect to the data. This, in turn, is based on the

presumed accuracy of the PC surrogate. The procedure outlined above is the essence of the idea put forth in [19]. It yields significant computational savings over the direct approach (2.6), since the latter requires a full MD simulation, whereas evaluating M_k in (2.11) simply amounts to a polynomial substitution.

In the present work, we treat the variances $\tilde{\sigma}^2 = \{\tilde{\sigma}_k^2\}_{k=1}^3$ as hyperparameters. Bayes's theorem yields the following joint posterior:

$$(2.12) \quad \pi(\boldsymbol{\xi}, \tilde{\sigma}^2 \mid \{G_l\}_{l=1}^3) \propto \prod_{k=1}^3 \prod_{i=1}^N \frac{\exp\left(-\frac{[G_k^i - M_k(\boldsymbol{\xi})]^2}{2\tilde{\sigma}_k^2}\right)}{\sqrt{2\pi\tilde{\sigma}_k^2}} \tilde{q}(\tilde{\sigma}_k^2) q(\boldsymbol{\xi}),$$

where $\tilde{q}(\tilde{\sigma}_k^2)$ is the prior of the noise variance, $\tilde{\sigma}_k^2$, and $q(\boldsymbol{\xi})$ represents the probability in the $\boldsymbol{\xi}$ -space corresponding to the prior on the parameter vector $\boldsymbol{\theta} = \{\varepsilon, \sigma, d\}$. Note that since the transformation, \mathbf{f} , used in (2.8) is affine, the multiplicative term involving the Jacobian of \mathbf{f} associated with the change of variables from the $\boldsymbol{\theta}$ -space to the $\boldsymbol{\xi}$ -space is a constant and is omitted from the right-hand side of (2.12). Note that we have used a tilde to distinguish between the variance, $\tilde{\sigma}_k^2$, associated with the k th observable and the force-field parameter, σ .

For the parameters $\boldsymbol{\theta}$, we assume a uniform prior with support equal to that defined by (2.7). Note that this choice is not unique since one could endow the parameters $\boldsymbol{\theta}$ with a more informative prior. The choice, however, has to satisfy two constraints: the support of the prior has to be contained within that defined by the expansion in (2.7), and the transformation \mathbf{f} has to be an invertible map. For the variances $\{\tilde{\sigma}_k^2\}_{k=1}^3$, leveraging the fact that their values cannot be negative, we assume a Jeffreys prior of the form

$$(2.13) \quad q(\tilde{\sigma}_k^2) = \frac{1}{\tilde{\sigma}_k^2}, \quad k = 1, 2, 3.$$

We sample the posterior (2.12) in the $\boldsymbol{\xi}$ -space with an adaptive Metropolis (AM) algorithm (see, e.g., [9, 2, 1, 29, 30]) of the form discussed in Part I. As the proposal distribution, Q , we adopt a multivariate Gaussian, centered around the current state and whose covariance matrix, \mathcal{C} , is built according to

$$(2.14) \quad \mathcal{C} = \begin{cases} \mathcal{C}_0 & \text{for } t < t_0, \\ \delta \text{Cov}_{1,2,\dots,t} & \text{for } t \geq t_0, \end{cases}$$

where t_0 defines the step at which the adaptation is triggered, \mathcal{C}_0 is the fixed covariance used for the initial steps, $\text{Cov}_{1,2,\dots,t}$ denotes the covariance computed using the samples collected by the chain during all previous steps, and δ is a parameter that must be fixed before running the chain and tuned to achieve good mixing to enable efficient exploration of the target distribution. Since (2.12) is a function of the uniform RVs $\boldsymbol{\xi}$, the results can then be inverted back in terms of the force-field parameters ε , σ , and d using (2.7). In the present work, we assume $t_0 = 500$ steps and each chain is run for 20000 steps with the associated burn-in period estimated based on the autocovariance function.

2.4.2. Nondeterministic surrogate model. In this subsection, we present the formulation of the problem using a surrogate model based on the *nondeterministic* PC expansions inferred in Part I. In this case, each set of PC coefficients $\mathbf{c}^{(k)} = \{c_l^{(k)}\}_{l=0}^P$, $k = 1, 2, 3$, of the expansions introduced in (2.9) is a random vector defined by a

$(P + 1)$ -dimensional joint probability density. As a consequence, the model prediction, $M_k(\xi)$, for each observable depends on two main contributions: the parametric uncertainty through the germ ξ , and the uncertainty in the PC coefficients stemming from the fact that the expansions were obtained via Bayesian inference from noisy MD observations.

We can define a suitable likelihood function for this case as follows. For a given sample $\xi^{(j)} = \{\xi_1^{(j)}, \xi_2^{(j)}, \xi_3^{(j)}\}$, we can construct the constant column vector

$$(2.15) \quad \mathbf{a} = \{\Psi_0(\xi^{(j)}), \dots, \Psi_P(\xi^{(j)})\}^T,$$

i.e., by substituting $\xi^{(j)}$ into the truncated PC basis. Hence, we can interpret each *nondeterministic* PC representation, $M_k(\xi)$, as a *linear combination* of the random vector $\mathbf{c}^{(k)}$ according to

$$(2.16) \quad M_k = \mathbf{a}^T \mathbf{c}^{(k)}, \quad k = 1, 2, 3.$$

For the present study, as shown in Part I, the probability density describing the uncertain PC expansion of each observable closely resembles a Gaussian. We thus approximate the $(P+1)$ -dimensional distribution describing the random vector $\mathbf{c}^{(k)} = \{c_0^{(k)}, \dots, c_P^{(k)}\}^T$, $k = 1, 2, 3$, with a $(P+1)$ -variate Gaussian with mean $\boldsymbol{\mu}^{(k)}$ and covariance matrix $\mathbf{Z}^{(k)}$, $k = 1, 2, 3$. The mean vectors and covariance matrices can be directly computed from the MCMC samples obtained in Part I. Consequently, the linear combination

$$(2.17) \quad \mathbf{a}^T \mathbf{c}^{(k)} = \Psi_0(\xi^{(j)}) c_0^{(k)} + \dots + \Psi_P(\xi^{(j)}) c_P^{(k)}, \quad k = 1, 2, 3,$$

is distributed according to a *univariate* Gaussian with mean $(\mathbf{a}^T \boldsymbol{\mu}^{(k)})$ and variance $(\mathbf{a}^T \mathbf{Z}^{(k)} \mathbf{a})$, $k = 1, 2, 3$; in short notation this is expressed as

$$(2.18) \quad \mathbf{a}^T \mathbf{c}^{(k)} \sim \mathcal{N}\left(\mathbf{a}^T \boldsymbol{\mu}^{(k)}, \mathbf{a}^T \mathbf{Z}^{(k)} \mathbf{a}\right), \quad k = 1, 2, 3.$$

Note that the uncertainty in the PC coefficients appears only through the mean vector $\boldsymbol{\mu}^{(k)}$ and the covariance $\mathbf{Z}^{(k)}$ since the constant vector \mathbf{a} is only ξ -dependent. Assuming an independent additive error model, the discrepancy between each observation, G_k^i , $k = 1, 2, 3$, $i = 1, \dots, N$, and the *nondeterministic* surrogate model prediction, $M_k(\xi) = \mathbf{a}^T \mathbf{c}^{(k)}$, $k = 1, 2, 3$, can be expressed as

$$(2.19) \quad \begin{aligned} G_k^i &= M_k(\xi) + \gamma_k^i \\ &= \mathbf{a}^T \mathbf{c}^{(k)} + \gamma_k^i, \quad k = 1, 2, 3, \quad i = 1, \dots, N, \end{aligned}$$

where each set $\{\gamma_k^i\}_{i=1}^N$, $k = 1, 2, 3$, comprises i.i.d. RVs with density p_{γ_k} , $k = 1, 2, 3$. Assuming $\gamma_k^i \sim \mathcal{N}(0, \tilde{\sigma}_k^2)$, $i = 1, \dots, N$, $k = 1, 2, 3$, and considering, by construction, N independent realizations for each observable, G_k , $k = 1, 2, 3$, we obtain the following likelihood function:

$$(2.20) \quad \mathcal{L}(\xi; \{\mathbf{G}_l\}_{l=1}^3) = \prod_{k=1}^3 \prod_{i=1}^N \frac{1}{\sqrt{2\pi (\mathbf{a}^T \mathbf{Z}^{(k)} \mathbf{a} + \tilde{\sigma}_k^2)}} \exp\left(-\frac{[G_k^i - (\mathbf{a}^T \boldsymbol{\mu}^{(k)})]^2}{2(\mathbf{a}^T \mathbf{Z}^{(k)} \mathbf{a} + \tilde{\sigma}_k^2)}\right),$$

where the index k enumerates the observables, i enumerates the observations, $\boldsymbol{\mu}^{(k)}$ and $\mathbf{Z}^{(k)}$, respectively, denote the mean and covariance matrix of the $(P + 1)$ -variate Gaussian representing the $(P + 1)$ -dimensional distribution of the *nondeterministic* PC coefficients featured in the expansion of the k th observable, and the constant vector $\mathbf{a} = \{\Psi_0(\xi), \dots, \Psi_P(\xi)\}^T$ is computed by evaluating the PC basis for a given ξ . Consistent with section 2.4.1, we treat the variances $\tilde{\sigma}^2 = \{\tilde{\sigma}_k^2\}_{k=1}^3$ as hyperparameters. It is noteworthy that the above likelihood function combines both data noise and surrogate uncertainty in a self-consistent manner. For each data point, the likelihood reaches its maximum if the data and the surrogate mean coincide. Deviations from this mean are weighted by the sum of variances of the noise *and* the uncertain surrogate. Accordingly, regions of high data noise or large surrogate uncertainty are both penalized with lower weighting on discrepancies between the data and the mean-surrogate model.

Using Bayes's theorem, the joint posterior distribution is given by

$$(2.21) \quad \pi(\xi, \tilde{\sigma}^2 \mid \{\mathbf{G}_l\}_{l=1}^3) \propto \mathcal{L}(\xi; \{\mathbf{G}_l\}_{l=1}^3) \tilde{q}(\tilde{\sigma}^2) q(\xi),$$

where, as before, the additional multiplicative term, involving the Jacobian of the affine transformation \mathbf{f} (see (2.8)), is a constant and is omitted from the right-hand side of (2.21). For the priors, we adopt the same approach outlined in section 2.4.1, and the posteriors (2.21) are sampled using an AM algorithm, as described in (2.14). The results are inverted back in terms of the force-field parameters ε , σ , and d using (2.7).

3. Results.

3.1. Deterministic surrogate. In this subsection, we discuss the results of the inverse problem obtained with a *deterministic* PC expansion as the surrogate model.

3.1.1. Inference based on a single observable. As a first test case, we run the inverse problem described in section 2.4.1 only in terms of density, ρ , neglecting the observations collected for self-diffusivity and enthalpy. Consequently, the joint posterior (2.12) reduces to

$$(3.1) \quad \pi(\xi, \tilde{\sigma}_1^2 \mid \mathbf{G}_1) \propto \prod_{i=1}^N \frac{1}{\sqrt{2\pi\tilde{\sigma}_1^2}} \exp\left(-\frac{[G_1^i - M_1(\xi)]^2}{2\tilde{\sigma}_1^2}\right) \tilde{q}(\tilde{\sigma}_1^2) q(\xi),$$

where $\mathbf{G}_1 = \{G_1^i\}_{i=1}^N$ is the set of observations collected for density shown in Figure 2.2(a), while $M_1(\xi)$ is the p th-order *deterministic* PC representation of density computed in Part I using NISP.

Figures 3.1(a)–(c) show the chain samples obtained for the inferred force-field parameters ε (a), σ (b), and d (c) using a third-order ($p = 3$) surrogate model and $N = 10$ observations of density. For reference, a superimposed red line identifies the “true” parameters previously defined in (2.2). The plots show large uncertainties dominating the inferred parameters. Specifically, while the chains for σ and d describe wide oscillations spanning their entire range of variation (see Figures 3.1(b)–(c)), a narrower oscillation is observed for ε ; see panel (a). Figure 3.1(d) shows a 3D plot of the chain after removing a burn-in period of 3000 steps, with the superimposed red dot indicating the “true” parameter vector. The plot reveals that the chain samples distribute over a well-defined hyperplane in the space, which contains the “true” point but is characterized by a large uncertainty.

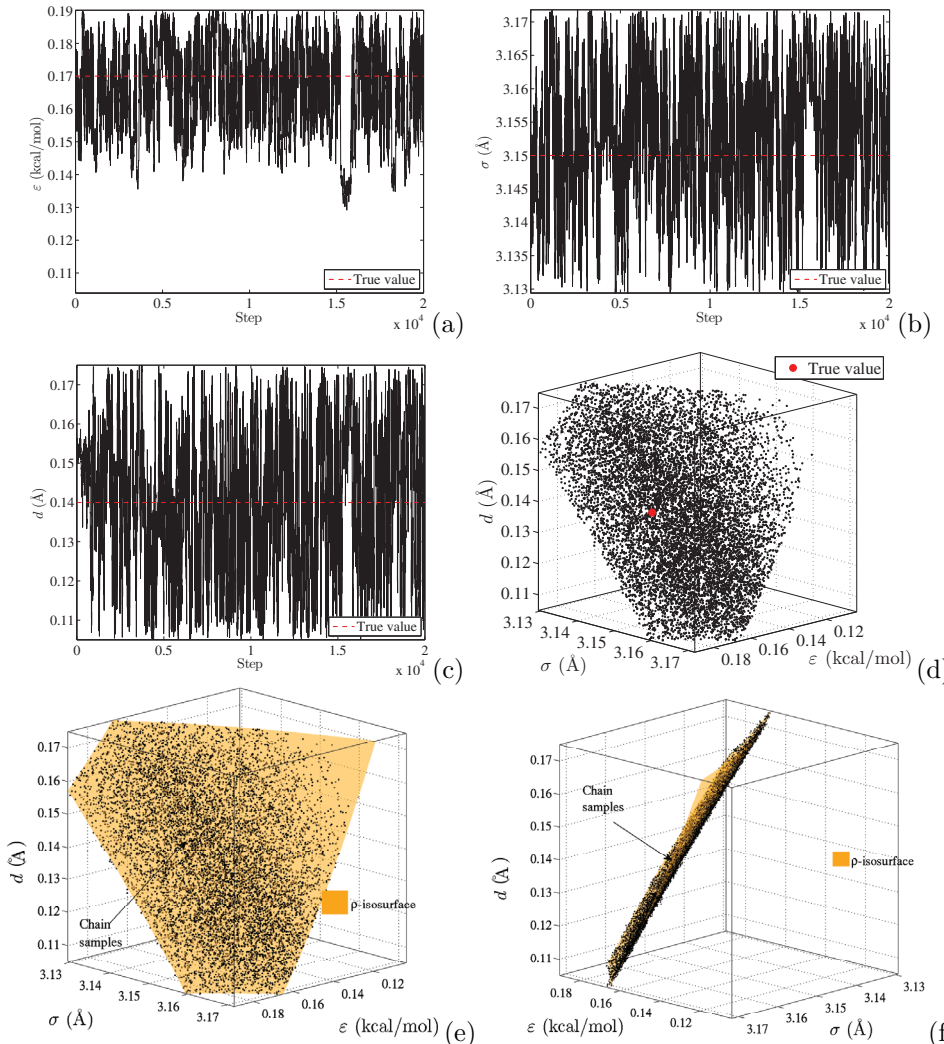


FIG. 3.1. Panels (a)–(c): chain samples (black, solid lines) for ε (a), σ (b), and d (c) obtained using $N = 10$ observations of density and a third-order deterministic surrogate model. The “true” values of the parameters are indicated by red, dashed lines. Panel (d): 3D plot of the chain (black dots) after removing a 3000-step burn-in period. The “true” parameter vector is indicated with a red dot. Panels (e) and (f) show two different views of the chain samples, as well as the surrogate isosurface $M_1(\xi) = \overline{G}_1$, where \overline{G}_1 is the mean value of the $N = 10$ observations of density shown in Figure 2.2(a).

Further insight into this result can be gained by analyzing Figures 3.1(e)–(f), showing two different views of the chain samples superimposed on the isosurface extracted from the PC surrogate, according to

$$(3.2) \quad M_1(\xi) = \overline{G}_1,$$

where $M_1(\xi)$ is the third-order *deterministic* surrogate for ρ and \overline{G}_1 is the mean value of the observations $\{G_{1,i}^i\}_{i=1}^{10}$ of density shown in Figure 2.2(a). In other words, we extract from the PC expansion the isosurface connecting points with values equal to

the mean value of the data $\{G_1^i\}_{i=1}^{10}$. Figures 3.1(e)–(f) reveal that the hyperplane outlined by the chain coincides with the isosurface defined above, suggesting that (3.2) plays a key role in determining the posterior distribution. This result explains why the amplitude of the oscillations observed for ε is smaller than that characterizing σ and d , as shown by panels (a)–(c). This is due to the orientation and spread of the isosurface. While the isosurface defined above spans the entire range of variation of σ and d , its spread along ε is narrower than the axis range, inducing narrower oscillations for ε . The above observations indicate that a single observable yields an underdetermined problem, where two degrees of freedom appear to be missing. For brevity, the results obtained using self-diffusivity or enthalpy are omitted from the present manuscript only because they yield similar conclusions.

3.1.2. Inference based on three observables. We now discuss the results obtained for the inverse problem when the observations for all three observables (ρ, D, H) are considered. In this case, the target posterior has the form in (2.12).

Figures 3.2(a)–(c) show the chain samples obtained for ε (a), σ (b), and d (c) computed using a third-order surrogate model and a total of 30 observations, i.e., $N = 10$ for each observable. In this case, the chain locates the “true” parameters and exhibits small-amplitude oscillations, reflecting a considerable reduction in the posterior uncertainty with respect to the results based on a single observable.

Figure 3.2(d) shows a 3D view of the chain samples after removing a burn-in period of 5000 steps. The figure reveals that the chain explores a narrow region centered around the “true” parameter vector, indicated with a red dot. This is further analyzed in Figures 3.2(e)–(f), which show two different views of the chain superimposed on the three isosurfaces extracted from the surrogate model, according to

$$(3.3) \quad M_k(\xi) = \overline{\mathbf{G}}_k, \quad k = 1, 2, 3,$$

where $\overline{\mathbf{G}}_k$ is the mean value of the observations $\{G_k^i\}_{i=1}^{10}$ obtained for the k th observable shown in Figure 2.2. The three isosurfaces intersect at a single point, covering all the degrees of freedom, and, thus, the problem is well defined.

Posterior densities and sensitivity analysis. We now investigate how the results of the inference depend on the order, p , of the surrogate model and on the number, N , of observations considered for each observable. To discuss this sensitivity analysis, we rely on the marginalized posteriors of the inferred parameters.

The first column of Figure 3.3 shows the kernel density estimation (KDE) of the marginalized posteriors $\pi(\varepsilon)$ (a), $\pi(\sigma)$ (c), and $\pi(d)$ (e) inferred using a third-order surrogate model and $3N = 9, 15, 24$, and 30 total observations, i.e., $N = 3, 5, 8$, and 10 data points for each observable. We superimpose a dashed line to indicate the “true” value of each parameter. The shape of the posterior strongly depends on the total number, $3N$, of observations. As $3N$ increases from 9 to 30, the variances of the marginalized posteriors of all three parameters decrease in a monotonic fashion. This trend is expected because increasing the number of data points reflects additional information, and, thus, less uncertainty is projected in the results. A different trend is observed for the maximum a posteriori (MAP) estimate of the inferred parameters. Figures 3.3(a), (c), and (e) show that the MAP estimate of each parameter is minimally affected by the total number, $3N$, of observations. For all three parameters, indeed, the MAP estimates computed from the two limiting cases, i.e., those with 9 and 30 total observations, differ at most by 2%. For the other cases, the variations are even smaller. Finally, we examine the discrepancy between the MAP estimates and the “true” values of the parameters. Figures 3.3(a), (c), and (e)

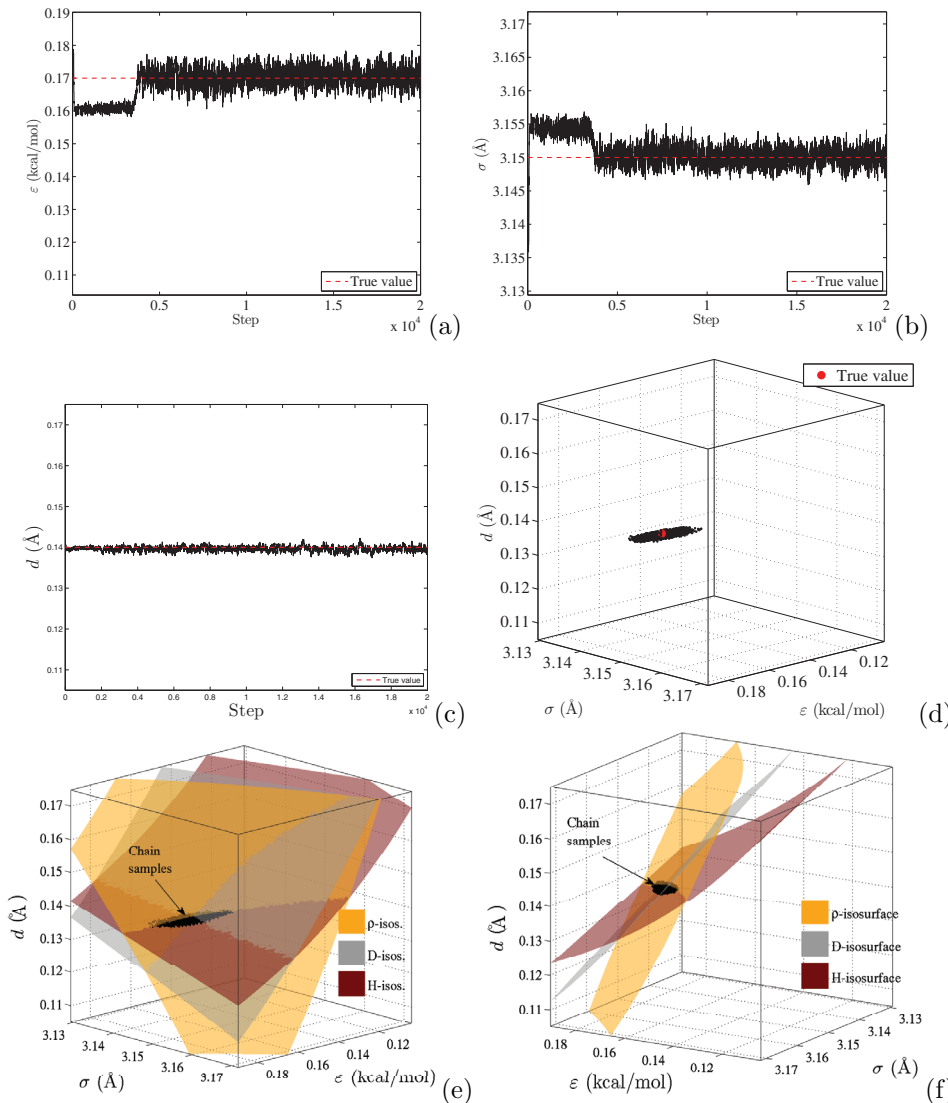


FIG. 3.2. Panels (a)–(c): chain samples (black, solid lines) for ε (a), σ (b), and d (c) obtained using a third-order ($p = 3$) deterministic surrogate model for (ρ, D, H) and a total of 30 observations, i.e., $N = 10$ for each observable. The “true” values of the parameters are indicated with red dashed lines. Panel (d): 3D plot of the chain (black dots) after removing a 5000-step burn-in period. The “true” parameter vector is indicated with a red dot. Panels (e) and (f) show two different views of the chain samples, as well as surrogate isosurfaces $M_k(\xi) = \overline{\mathbf{G}}_k$, $k = 1, 2, 3$, where $\overline{\mathbf{G}}_k$ is the mean value of the 10 observations of the k th observable shown in Figure 2.2.

show that this discrepancy is close to zero for the case involving 30 total observations and increases slightly for the results based on 9, 15, and 24 observations. Overall, however, in all cases the differences can be considered quite small.

Next, we analyze how the results of the inference depend on the order, p , of the surrogate model for a given a number of observations. The second column of Figure 3.3 shows the KDE of the marginalized posteriors $\pi(\varepsilon)$ (b), $\pi(\sigma)$ (d), and $\pi(d)$ (f) inferred using 30 total observations and a surrogate PC model with order $2 \leq p \leq 6$. The plots

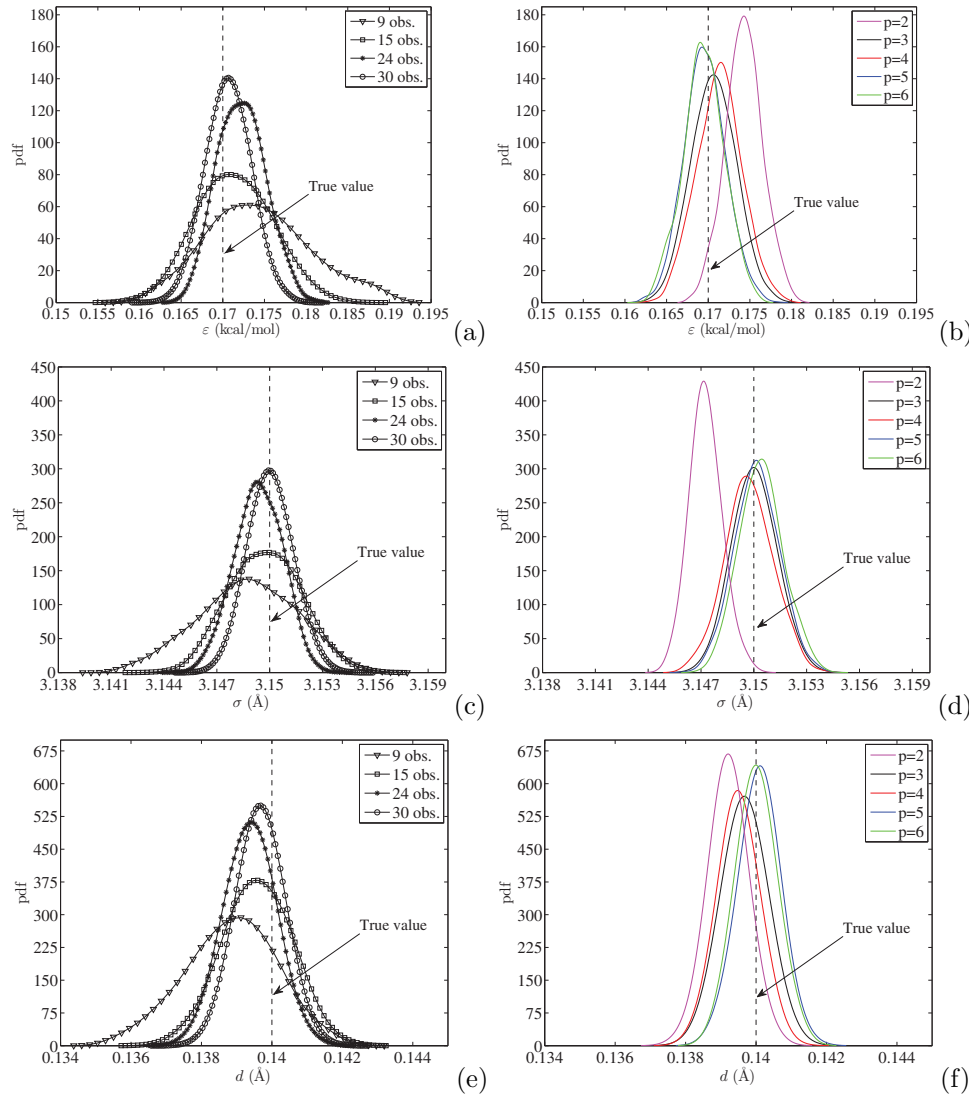


FIG. 3.3. Left column: KDE of the marginalized posteriors $\pi(\varepsilon)$ (a), $\pi(\sigma)$ (c), and $\pi(d)$ (e) obtained using a third-order deterministic surrogate model for (ρ, D, H) , based on $3N = 9, 15, 24$, and 30 total observations. Right column: KDE of $\pi(\varepsilon)$ (b), $\pi(\sigma)$ (d), and $\pi(d)$ (f) computed using different order expansions as indicated. A deterministic surrogate model for (ρ, D, H) is used, based on a total of 30 observations.

show that a quadratic surrogate yields marginalized posteriors that are slightly shifted with respect to those based on higher-order ($p \geq 3$) representations; see Figures 3.3(b), (d), and (f). Specifically, the quadratic surrogate yields an overestimation for ε (see panel (b)), while an underestimation is observed for σ and d ; see panels (d) and (f). To evaluate the accuracy of the inference, we analyze the discrepancy between the MAP estimates of the inferred parameters and the corresponding “true” values. For all orders explored, these discrepancies are less than 3% and, thus, are relatively small. Figures 3.3(b), (d), and (f) reveal, also, that the posteriors obtained for $p \geq 3$ are very

close one to another. This is particularly evident if we analyze their MAP estimates, showing, indeed, no substantial variation as the order, p , of the surrogate increases from $p = 3$ to $p = 6$; see panels (b), (d), and (f). Minor differences, however, arise in their variances. The posterior variance of each parameter remains nearly unchanged when using third- and fourth-order expansions and decreases slightly for $p = 5$ and 6. The above analysis suggests that while the MAP estimates of the inferred parameters are not particularly sensitive to the order of the surrogate model when using $p \geq 3$, the variance decreases slightly when using expansions of order $p \geq 5$.

Correlation structure. We now focus on the correlations arising between the inferred parameters. This is motivated by the fact that the latter plays, in general, a key role in characterizing the corresponding model predictions, especially when the problem under consideration exhibits strong nonlinearities (see, e.g., [20] and the references therein). To this end, we leverage the 3D marginalized joint posterior, $\pi(\varepsilon, \sigma, d)$, to obtain two-dimensional (2D) joint posteriors for each possible combination of the parameters, namely $\pi(\varepsilon, \sigma)$, $\pi(\varepsilon, d)$, and $\pi(\sigma, d)$. In the present case, it is especially instructive to analyze the correlation between the two LJ parameters, ε and σ , and, also, their individual correlation with the geometric parameter, d . This can be useful for gaining some insight into their mutual dependence.

Figures 3.4(a), (c), and (e) show the scatter plots of 15000 samples of (ε, σ) (a), (ε, d) (c), and (σ, d) (e) obtained from the chain samples of the marginalized posterior inferred with a third-order *deterministic* surrogate model, based on 30 total observations (i.e., $N = 10$ for each observable). The 15000 samples originate from the fact that a burn-in period of 5000 steps is removed from the original chains before plotting the data. The plots reveal a strong correlation in all three cases. Specifically, whereas (ε, σ) and (ε, d) exhibit a negative correlation structure and define a quite narrow distribution (see panels (a) and (c)), the samples of (σ, d) shows a positive correlation and an overall wider spread. These samples can be readily exploited to reconstruct the joint density for each combination of parameters. The right column of Figure 3.4 shows the contour plots of the marginalized joint posteriors $\pi(\varepsilon, \sigma)$ (b), $\pi(\varepsilon, d)$ (d), and $\pi(\sigma, d)$ (f). A black line is used for the contours obtained from the distribution reconstructed via KDE, while a red line is used for the contours obtained from a bivariate Gaussian with mean and covariance estimated from the samples. The plots show that the KDE-based joint posteriors are in very good agreement with the Gaussian-based results. A minimal difference is reflected in the fact that the Gaussian-based contours are slightly narrower than the black ones. Overall, however, these discrepancies are quite small, allowing us to conclude that the marginalized joint posteriors can be suitably approximated by Gaussian distributions.

To quantify the degree of correlation between each possible pair of parameters, we compute the correlation coefficients $\zeta(\varepsilon, \sigma)$, $\zeta(\varepsilon, d)$, and $\zeta(\sigma, d)$, and plot the results in Figure 3.5 against the order of the surrogate model, for $p = 2, \dots, 6$. The correlation coefficient, $\zeta(X, Y)$, between two random variables X and Y is defined as

$$(3.4) \quad \zeta(X, Y) = \frac{\mathbb{E}[(X - \mu_X)(Y - \mu_Y)]}{\sigma_X \sigma_Y},$$

where \mathbb{E} is the expectation operator, while (μ_X, σ_X) and (μ_Y, σ_Y) are means and standard deviation values for X and Y , respectively. The correlation coefficient falls in the range $(-1, 1)$, with 1 indicating a perfect positive correlation and -1 for a case of perfect negative correlation. Figure 3.5 shows that for all three combinations of parameters considered, the order, p , of the surrogate model has a substantial effect on ζ . Specifically, going from a quadratic to a cubic surrogate yields a sharp variation in

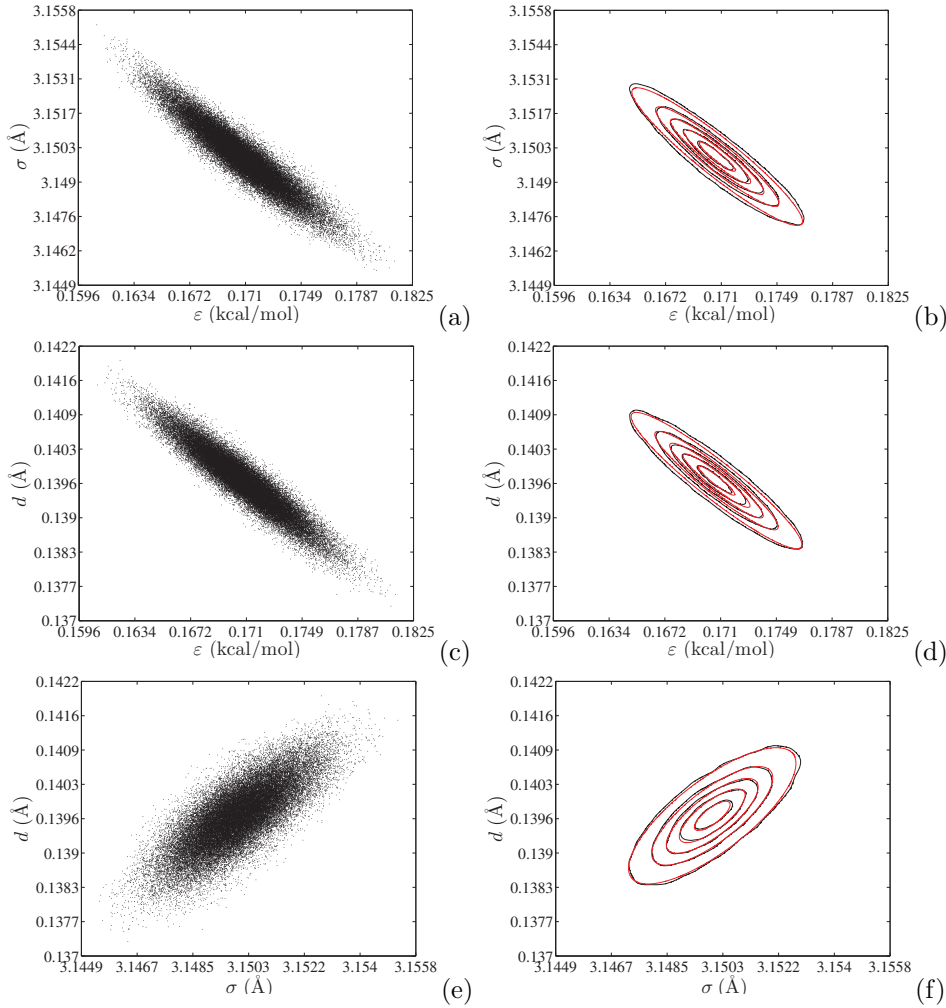


FIG. 3.4. Left column: scatter plots of (ε, σ) (a), (ε, d) (c), and (σ, d) (e) obtained from the chain samples (Figure 3.2) of the corresponding marginalized joint posterior inferred using a third-order deterministic surrogate model based on 30 total observations. Right column: contour plots of $\pi(\varepsilon, \sigma)$ (b), $\pi(\varepsilon, d)$ (d), and $\pi(\sigma, d)$ (f). The black line denotes results obtained via KDE, whereas the red line represents bivariate Gaussian results, with mean and covariance estimated from the samples. The contours correspond to 10%, 30%, 50%, 70%, and 90% of the maximum probability.

ζ . However, for surrogates of order $p \geq 3$, ζ tends to fluctuate around a well-defined mean value. This further supports the previous claim that a surrogate of order $p \geq 4$ yields no considerable improvement in the results. To provide a single measure of the correlation for each case, we take the values of ζ obtained for $3 \leq p \leq 6$ and calculate their mean, obtaining the following numerical estimates: $\zeta(\varepsilon, \sigma) \approx -0.944$, $\zeta(\varepsilon, d) \approx -0.932$, and $\zeta(\sigma, d) \approx 0.766$. These values suitably reflect the structure observed for the distributions in the second column of Figure 3.4. Indeed, while the two posteriors $\pi(\varepsilon, \sigma)$ and $\pi(\varepsilon, d)$ are very sharp and elongated (see Figures 3.4(b) and (d)), resulting in an absolute value of ζ close to unity, the posterior $\pi(\sigma, d)$ is broader (see Figure 3.4(f)), leading to a smaller absolute value of ζ .

It is important to remark that the correlation between the inferred parameters is

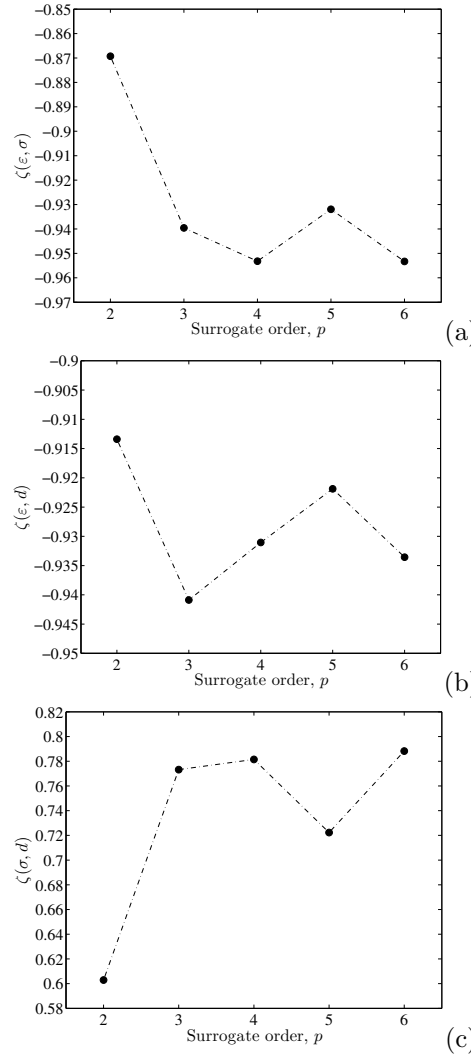


FIG. 3.5. (a) Correlation coefficient, $\zeta(\varepsilon, \sigma)$, versus the order, p , of the deterministic surrogate model. The correlation coefficient is computed for the marginalized joint posterior $\pi(\varepsilon, \sigma)$ inferred using 30 total observations of (ρ, D, H) . Panels (b) and (c) show the corresponding results obtained for $\zeta(\varepsilon, d)$ and $\zeta(\sigma, d)$, respectively.

information that was missing prior to the inference. In fact, since the three parameters were initially assumed to be independent in (2.7), their correlation was identically zero. The inference, on the other hand, suggests that a significant degree of correlation exists between these three force-field parameters. This stems from the forward model solution and is manifested during the inference based on the corresponding PC surrogate.

3.2. Nondeterministic surrogate. In this subsection, we present the results of the inverse problem obtained with a *nondeterministic* surrogate model, using the formulation of section 2.4.2. We recall that the key feature distinguishing a *deterministic* from a *nondeterministic* PC expansion is that the latter involves uncertainty in the

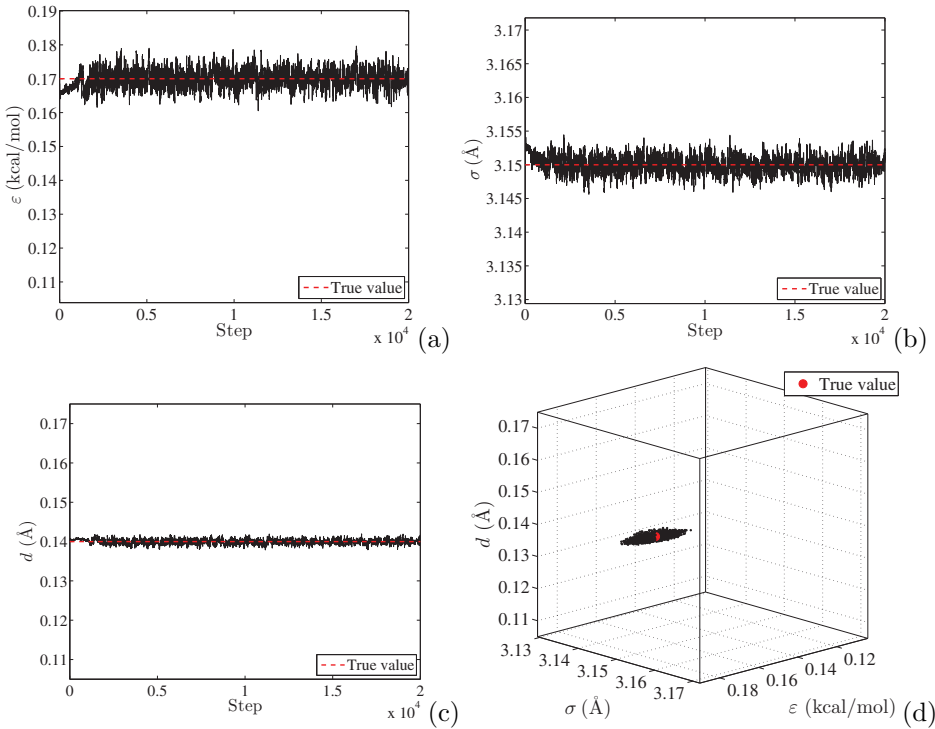


FIG. 3.6. Panels (a)–(c): chain samples (black, solid lines) obtained for ε (a), σ (b), and d (c), based on a third-order nondeterministic surrogate model for (ρ, D, H) with $\lambda = 0$. The “true” values of the parameters are indicated with red dashed lines. The results are based on 30 observations, i.e., $N = 10$ for each observable. Panel (d) shows the 3D plot of the chain samples after removing a 3000-step burn-in period. The “true” parameter vector is indicated with a red dot.

surrogate due to the MD sampling noise in the observables from which it was derived, and this uncertainty is characterized by making the spectrum of coefficients a random vector with a well-defined joint distribution. Uncertain PC expansions for the observables of interest, ρ , D , and H , were obtained in Part I using Bayesian inference. We built these *nondeterministic* PC expansions demonstrating a new technique, based on Fejér nested grids, to collect realizations by adaptively sampling the parameter space. Within this sampling strategy, we introduced a parameter, $0 \leq \lambda \leq 1$, having the role of a tolerance that determines the number of selected sampling points in the reduced grid with respect to the original Fejér grids. In particular, we explored three values of λ , namely $\lambda = 0$, 0.25, and 0.40. The reader is referred to sections 3.2 and 4.2 of [28] for the details of the construction of these PC representations. Below, we will discuss the results of the inverse problem based on the resulting *nondeterministic* surrogates with particular emphasis on the effects of λ .

Figures 3.6(a)–(c) show the chain samples for the inferred parameters ε (a), σ (b), and d (c) based on a third-order *nondeterministic* PC surrogate with $\lambda = 0$ and using 30 total observations for (ρ, D, H) , i.e., $N = 10$ for each observable. For reference, the red line indicates the “true” values of the parameters introduced in (2.2). The chain shows good mixing properties, with a burn-in period of approximately 3000 steps. In particular, note that the oscillations observed for ε , σ are wider than those for d . Figure 3.6(d) presents the 3D plot of the chain samples after removing the burn-in

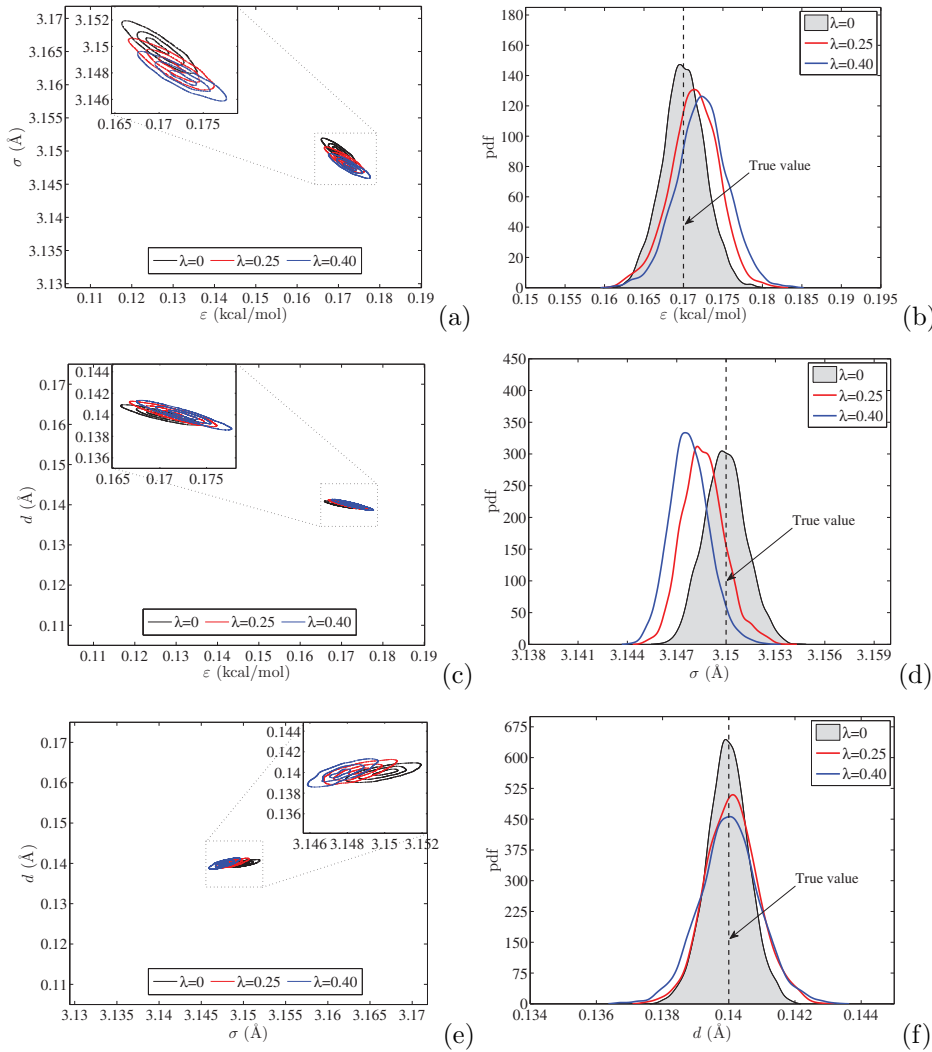


FIG. 3.7. Left column: contour plots corresponding to 30%, 60%, and 90% of the maximum probability of the marginalized joint posteriors $\pi(\varepsilon, \sigma)$ (a), $\pi(\varepsilon, d)$ (c), and $\pi(\sigma, d)$ (e) computed using a third-order nondeterministic surrogate model for (ρ, D, H) with $\lambda = 0$ (black line), $\lambda = 0.25$ (red), and $\lambda = 0.40$ (blue). Right column: KDE of the marginalized posteriors $\pi(\varepsilon)$ (b), $\pi(\sigma)$ (d), and $\pi(d)$ (f). The “true” values are indicated using dashed lines. The results are based on 30 total observations, namely $N = 10$ for each observable.

steps. The chain locates exactly the true parameter vector (red dot) and efficiently explores a neighboring region.

Sensitivity to the surrogate model. To investigate the impact of the tolerance parameter, we present in Figure 3.7 the contour plots of the marginalized joint posteriors $\pi(\varepsilon, \sigma)$ (a), $\pi(\varepsilon, d)$ (c), and $\pi(\sigma, d)$ (e) obtained using a third-order *nondeterministic* surrogate model with $\lambda = 0$ (black line), $\lambda = 0.25$ (red), and $\lambda = 0.40$ (blue). The contours correspond to 30%, 60%, and 90% of the maximum probability of the posteriors reconstructed with KDE. The results are based on 30 total observations for (ρ, D, H) , namely $N = 10$ data points for each observable. The plots reveal a high degree of

correlation for each combination of parameters, consistently with the results found with the deterministic surrogate. As λ increases from 0 to 0.40, the contours tend to widen, indicating a slightly larger uncertainty in the joint densities. The orientations of the joint posteriors also vary as λ changes. For $\pi(\varepsilon, \sigma)$, as λ increases from 0 to 0.40, the inclination of the joint posterior with respect to the horizontal axis reduces; see panel (a). The trend reverses for $\pi(\varepsilon, d)$ and $\pi(\sigma, d)$, where the inclination of the posterior with respect to the horizontal axis becomes sharper for increasing values of λ ; see panels (c) and (e).

Table 3.1 shows the correlation coefficients $\zeta(\varepsilon, \sigma)$, $\zeta(\varepsilon, d)$, $\zeta(\sigma, d)$ as a function of λ . As λ increases from 0 to 0.40, the variations in the coefficient are of order 0.5% for (ε, σ) , 4% for (ε, d) , and 12% for (σ, d) . Moreover, as previously noticed, whereas $\zeta(\varepsilon, \sigma)$ decreases in absolute value for increasing values of λ , the magnitude of $\zeta(\varepsilon, d)$ and $\zeta(\sigma, d)$ increases with λ .

TABLE 3.1

Correlation coefficients $\zeta(\varepsilon, \sigma)$, $\zeta(\varepsilon, d)$, $\zeta(\sigma, d)$ computed from the corresponding marginalized joint posteriors shown in the first column of Figure 3.7. The results are based on 30 total observations, namely $N = 10$.

	$\zeta(\varepsilon, \sigma)$	$\zeta(\varepsilon, d)$	$\zeta(\sigma, d)$
$\lambda = 0$	-0.92231	-0.93484	0.72866
$\lambda = 0.25$	-0.91915	-0.95463	0.76209
$\lambda = 0.40$	-0.91781	-0.97335	0.81885

To explore the effects of λ on each parameter individually, we present in the right column of Figure 3.7 the marginalized posteriors $\pi(\varepsilon)$ (b), $\pi(\sigma)$ (d), and $\pi(d)$ (f) computed for $\lambda = 0$ (shaded gray), $\lambda = 0.25$ (red), and $\lambda = 0.40$ (blue) and superimposed to the corresponding “true” values. Figures 3.7(b) and (f) show that the variances of $\pi(\varepsilon)$ and $\pi(d)$ monotonically increase as λ increases from 0 to 0.40. However, the variance of $\pi(\sigma)$ monotonically decreases as λ increases from 0 to 0.40. This result can be explained in terms of the inclination of the joint posteriors shown in the left column. Figure 3.7(a) shows, indeed, that the inclination of $\pi(\varepsilon, \sigma)$ with respect to the ε -axis decreases as λ increases from 0 to 0.40, while, at the same time, minimal changes affect the elongation. Consequently, as λ varies from 0 to 0.40, the uncertainty reduces along the σ -axis and increases for ε . A similar consideration can be made concerning the trends observed in panel (f).

Figures 3.7(b), (d), and (f) show that for the case $\lambda = 0$, the MAP estimates obtained for all three parameters are in very good agreement with their “true” values. The discrepancy increases slightly for the cases $\lambda = 0.25$ and 0.40 . To demonstrate that these differences are minimal overall, we report in Table 3.2 the nominal values of the MAP estimates of the parameters and the corresponding percentage error with respect to the “true” values (first row). The data are reported as a function of λ . The maximum discrepancy reaches nearly 1.4% when a surrogate with $\lambda = 0.40$ is used to infer ε , whereas it remains below 1% for all the other cases. The above observations allow us to conclude that while λ minimally affects the MAP estimates of the inferred parameters, yielding, in all cases, a very good agreement with the “true” values of the force-field parameters, it has a more significant effect on the posterior marginal variances.

3.3. Sensitivity of the inference to the choice of the observables. In the previous two sections, we discussed parameter inference based on *deterministic* and *nondeterministic* surrogates individually, focusing mainly on results obtained using

TABLE 3.2

Comparison between the “true” values of force-field parameters and the corresponding MAP estimates computed using the marginalized posteriors of the force-field parameters shown in the right column of Figure 3.7. The results are based on 30 total observations, namely $N = 10$ data points for each observable.

True values	$\hat{\varepsilon} = 0.17$		$\hat{\sigma} = 3.15$		$\hat{d} = 0.14$	
	MAP(ε)	Error, %	MAP(σ)	Error, %	MAP(d)	Error, %
$\lambda = 0$	0.16952	0.28235	3.14975	0.00794	0.13991	0.06428
$\lambda = 0.25$	0.17141	0.82941	3.14824	0.05587	0.14013	0.09286
$\lambda = 0.40$	0.17229	1.34706	3.14749	0.07968	0.14002	0.01428

observations for density alone and using all three observables together. We now aim at extending the analysis, namely by exploring the sensitivity of the inference to the type and number of observables considered. We restrict the discussion to results obtained using the *nondeterministic* surrogate. The analysis below was also performed using the *deterministic* surrogate, yielding similar results. For brevity, these are omitted.

The first step of this sensitivity analysis involves running the inference for several scenarios corresponding to using all possible combinations of the three available observables, ρ , D , and H . Seven different cases arise, which can be grouped into three different categories: first, we have three cases corresponding to taking each observable individually; second, we consider combinations of pairs of observables, namely (ρ, D) , (ρ, H) , and (D, H) ; finally, we have the scenario based on all three observables, (ρ, D, H) . To characterize the differences arising in the inference due solely to the choice of the observables, we constrain the *total* number of observations to remain (approximately) constant in each scenario. To this end, we consider $N = 10$ data points for each observable when taken individually, $N = 5$ for each observable used in paired combinations, and $N = 3$ for each of three observables in the last scenario. The total number of data points is thus maintained equal to 10 for all cases, except the last scenario, where we have 9. A third-order *nondeterministic* PC surrogate model is employed in all cases.

The left column of Figure 3.8 shows the marginalized posteriors $\pi(\varepsilon)$ (a), $\pi(\sigma)$ (c), and $\pi(d)$ (e) computed for the seven different scenarios above. The results are obtained using a cubic *nondeterministic* surrogate model with $\lambda = 0$. The plots clearly show that only the posteriors inferred using all three observables, (ρ, D, H) , display small variance and are sufficiently close to the “true” values for all three parameters. Specifically, the discrepancies between the MAP estimates and the “true” values are at most about 3%.

We now discuss each parameter individually. Panel (a), displaying the results for ε , shows that the first five scenarios investigated, i.e., those based on ρ , D , H , (ρ, D) , and (ρ, H) , yield posterior distributions that are nearly uniform over a support that slightly varies from one case to another. Since the prior on the parameters is uniform as defined by (2.7), it follows that these first five sets of observables yield little additional knowledge about ε with respect to its prior. On the contrary, the two cases based on (D, H) and (ρ, D, H) yield marginalized posteriors with Gaussian shape and smaller variance, and their MAP estimates fall close to the “true” value of ε . This suggests that the “true” value of ε can be recovered with sufficiently good accuracy using only two observables, (D, H) , rather than all three, (ρ, D, H) . The behavior of the marginalized posterior $\pi(\sigma)$ is similar. Figure 3.8(c) shows, in fact, that the inference scenarios based on ρ , D , H , and (D, H) produce corresponding

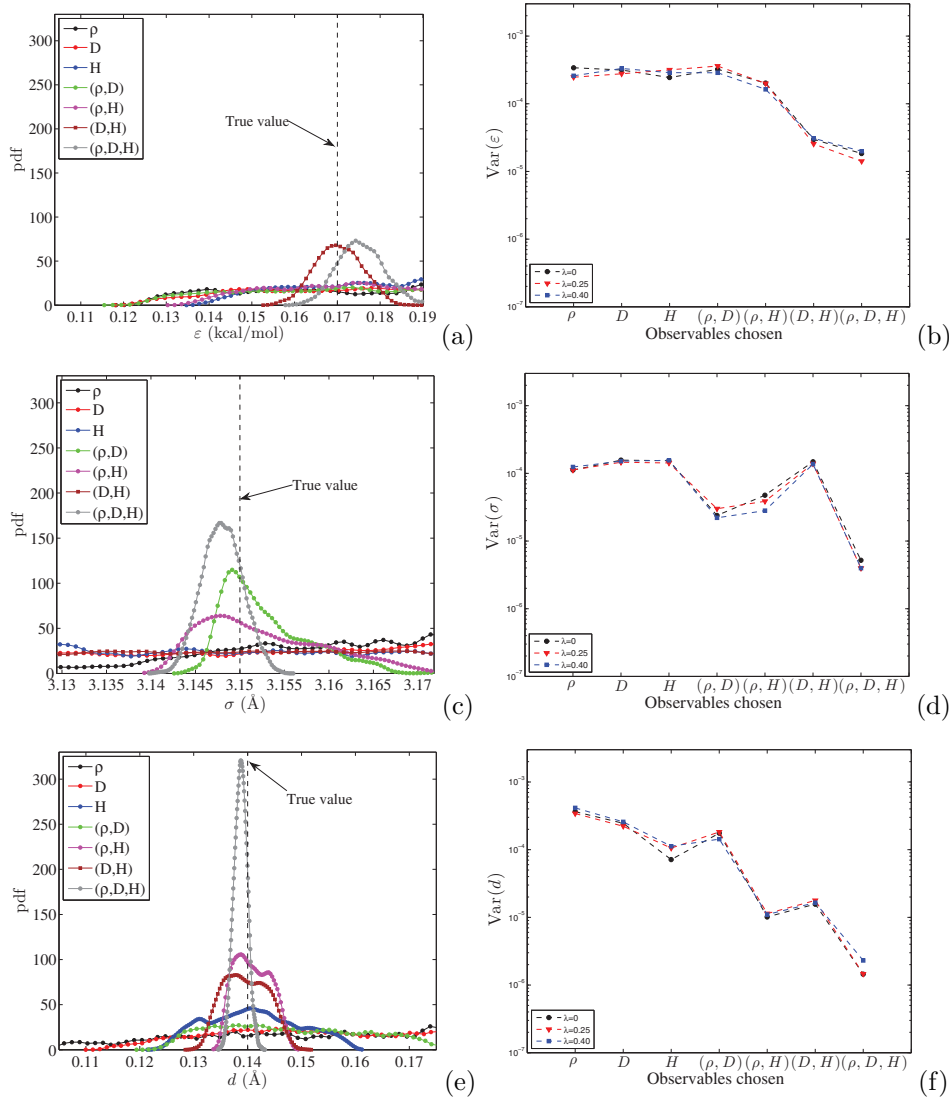


FIG. 3.8. Left column: KDE of the marginalized posteriors $\pi(\varepsilon)$ (a), $\pi(\sigma)$ (c), and $\pi(d)$ (e) obtained using different sets of observables and a third-order nondeterministic surrogate model with $\lambda = 0$. The right column shows the variances of the inferred parameters, $\text{Var}(\varepsilon)$ (b), $\text{Var}(\sigma)$ (d), and $\text{Var}(d)$ (f), plotted against the observables used. Curves are shown for $\lambda = 0$ (black), $\lambda = 0.25$ (red), and $\lambda = 0.40$ (blue). The results are obtained using $N = 10$ data points for the cases with a single observable, $N = 5$ (i.e., a total of 10) for those with a pair of observables, and $N = 3$ (i.e., a total of 9) when using all three, (ρ, D, H) .

posteriors resembling uniform densities over nearly the whole range of variation of σ . The results improve for (ρ, H) , (ρ, D) , and (ρ, D, H) . For these three cases, the marginalized posteriors become increasingly more Gaussian with decreasing variance. For the last parameter, d , Figure 3.8(e) shows that a nearly uniform posterior is obtained when using ρ , D , (ρ, D) , followed by a weak reduction of the variance when employing only H . Finally, the results substantially improve when the inference is run with (D, H) , (ρ, D) , and (ρ, D, H) . The above discussion suggests that each

parameter is very sensitive to certain sets of observables, while being only minimally affected by others. The choice of observables used in the inference may thus have a significant impact on the results.

The posterior variances corresponding to each scenario are plotted in the right column of Figure 3.8. Figures 3.8(b), (d), and (f) show how the variances of the inferred parameters, $\text{Var}(\varepsilon)$ (b), $\text{Var}(\sigma)$ (d), and $\text{Var}(d)$ (f), change as a function of the seven different inference scenarios explored. Depicted are results obtained using a third-order *nondeterministic* surrogate model with $\lambda = 0$ (black, circle), 0.25 (red, triangle), and 0.40 (blue, square). The results are consistent with the discussion above. Panels (b) and (d) show that $\text{Var}(\varepsilon)$ and $\text{Var}(\sigma)$ undergo a drop of one order of magnitude from their maxima to their minima. This fluctuation becomes even larger, two orders of magnitude, for $\text{Var}(d)$; see panel (f). Furthermore, note that, for a given parameter, the curves obtained for $\lambda = 0$, 0.25, and 0.40 outline a similar trend and display small differences. Again, this demonstrates that the effect of λ is present but overall weak.

We now discuss each parameter in detail. Panel (b) shows that $\text{Var}(\varepsilon)$ is nearly constant for the first four cases, i.e., ρ , D , H , and (ρ, D) , and subsequently drops by one order of magnitude to reach its global minimum for (ρ, D, H) . A different behavior is observed for $\text{Var}(\sigma)$. The trend is nearly flat for the three scenarios involving only ρ , D , or H , suddenly drops for (ρ, D) and (ρ, H) , increases rapidly again for (D, H) returning to the initial value, and then drastically decreases by two orders of magnitude to reach its global minimum for (ρ, D, H) . Finally, the behavior of $\text{Var}(d)$ shows variations even sharper than those observed for the previous two parameters, suggesting that d may be the force-field parameter most sensitive to the combination of observables used in the inference. Of course, the present discussion depends on the choice made in ordering the scenarios along the x -axis in Figures 3.8(b), (d), and (f), which, in the present case, is made according to the number of observables. However, common to all three parameters is that their variances reach a global minimum when all three observables (ρ, D, H) are used in the inference.

The present experience suggests that the output of the inference is intimately connected to the type and set of observables used but that this behavior is rooted in the structure of the model response. We illustrate this through a geometric analysis of the spatial interactions between the *nondeterministic* surrogate models for different sets of observables. For brevity, we present only three sample cases since a similar approach can be readily extended to the others. The left column of Figure 3.9 shows the 3D plots of the chain samples (black dots) obtained from the inference based on the three scenarios involving ρ (a), (ρ, H) (c), and (ρ, D, H) (e), in conjunction with a third-order *nondeterministic* surrogate model with $\lambda = 0$. As before, the results are obtained using 10 total observations for the cases ρ and (ρ, H) and 9 total data points for (ρ, D, H) . Superimposed on the chains, we display the isosurfaces extracted from the surrogate model, according to

$$(3.5) \quad \text{MAP}(M_k)(\xi) = \overline{\mathbf{G}}_k, \quad k = 1, 2, 3,$$

where $\text{MAP}(M_k)$ is the surrogate model obtained for the k th observable by setting the *nondeterministic* PC coefficients of the expansion with $\lambda = 0$ equal to their MAP estimates, while $\overline{\mathbf{G}}_k$ is the mean value of the corresponding observations. Figures 3.9(a), (c), and (e) show that the isosurfaces, particularly their intersections, impose a geometric constraint on the chain. The chain samples, indeed, are more densely clustered as we increase the number of observables considered in the inference. In the first case,

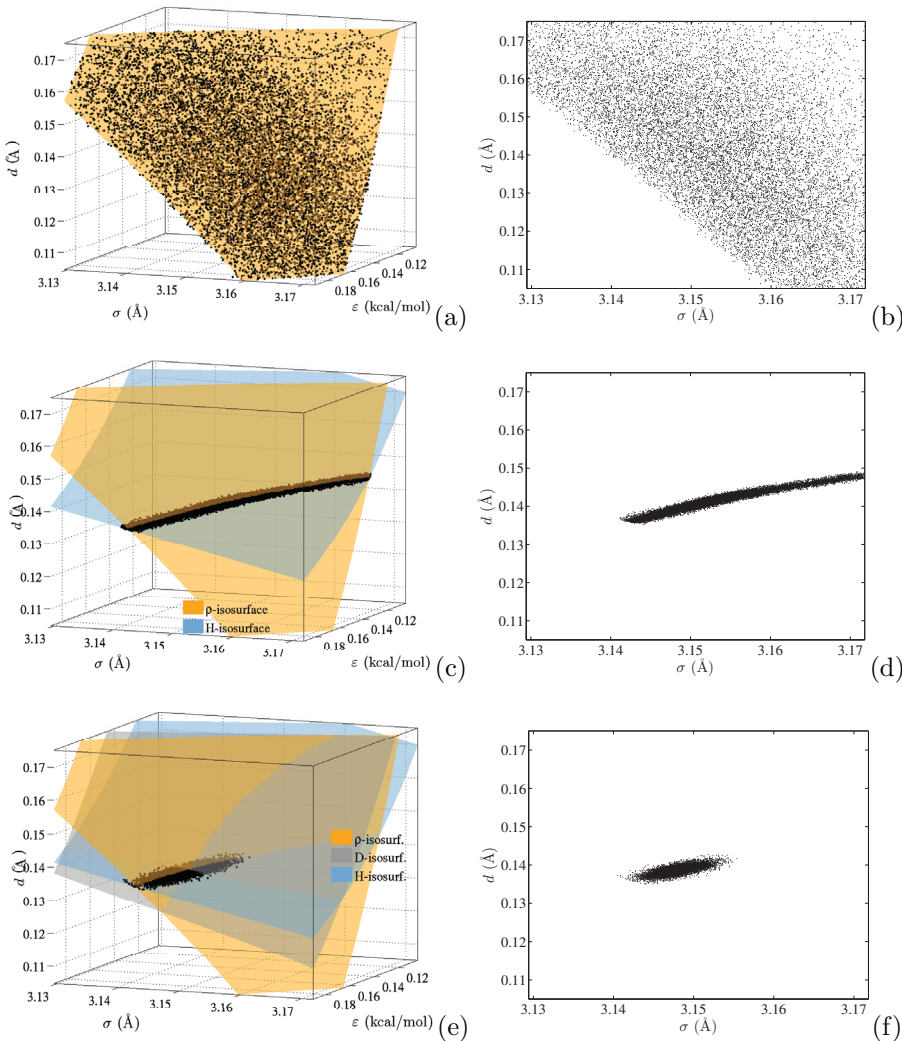


FIG. 3.9. Left column: 3D plots of the chain samples (black dots) obtained when inferring using ρ (a), (ρ, H) (c), and (ρ, D, H) (e). A third-order nondeterministic surrogate model with $\lambda = 0$ is used. Also shown are the isosurfaces extracted from the MAP estimates of the surrogate model. Right column: projected view of the chain samples on the (σ, d) -plane obtained for the inference based on ρ (b), (ρ, H) (d), and (ρ, D, H) (f). The results are computed using 10 total observations of ρ and (ρ, H) and 9 data points for (ρ, D, H) .

panel (a), the chain moves over the isosurface defined for density. When a second observable, D , is considered, the two resulting isosurfaces intersect and define a line in the 3D space that confines the chains. In the last case, panel (e), involving three observables, (ρ, D, H) , the three isosurfaces intersect at a point, and the resulting constraint on the chain is thus even tighter. By projecting these 3D plots of the samples on the 2D (σ, d) -plane, we obtain the plots in the right column of Figure 3.9. Large uncertainties dominate both σ and d in the first case; see panel (b). This result explains the nearly uniform posterior distributions obtained for σ and d in Figures 3.8(c) and (e) and, also, the corresponding large posterior variances observed in Figures 3.8(d)

and (f) when using only ρ . When the inference is based on two observables, (ρ, H) (see Figure 3.9(d)), the chain samples are more densely clustered along the (vertical) d -axis, while showing a wider spread along the (horizontal) σ -axis. This explains why using (ρ, H) yields the drastic drop in $\text{Var}(d)$ seen in Figure 3.8(f) and the corresponding weaker reduction obtained for $\text{Var}(\sigma)$; see Figure 3.8(d). Note that the chain samples in Figure 3.9(d) fall along a line that reaches the upper bound of σ , which is restricted by the prior. This result must consequently be deemed unsatisfactory because the chain is not suitably localized. In particular, the question remains open of whether consideration of broader bounds would significantly deteriorate the results.

Finally, when a third observable, H , is taken into account, Figure 3.9(f) shows that the geometric interplay of the surrogate models constrains the chain to explore a very narrow region around the intersection point, leading to a further drop in the posterior uncertainty of both d and σ . This explains why running the inference using (ρ, D, H) yields the global minima for $\text{Var}(\sigma)$ and $\text{Var}(d)$, as shown in Figures 3.8(e) and (f). The present considerations support the notion that the structure of the stochastic response surface plays a key role in determining the parameters' posteriors, and that useful information can be gained by analyzing this structure, prior to the inference or even the data collection.

3.3.1. Information gain. In this subsection, we analyze how the choice of the observables affects the information gain in the parameters, $\boldsymbol{\theta} = \{\varepsilon, \sigma, d\}$, by going from their prior, $q(\boldsymbol{\theta})$, to the posterior, $\pi(\boldsymbol{\theta})$, when the inference is run using a *nondeterministic* surrogate model. Specifically, we aim at determining which combination of observables yields the largest information gain in the parameters, providing us a proper guideline for favoring one choice over another.

We rely on the Kullback–Leibler (KL) divergence, $\Phi(\pi \| q)$, from the prior, $q(\boldsymbol{\theta})$, to the posterior, $\pi(\boldsymbol{\theta})$. We let $\pi_{(p=3,\lambda)}^A(\boldsymbol{\theta})$ be the marginalized joint posterior on the parameters obtained using a third-order *nondeterministic* surrogate model for a given λ and a specific set, A , of observables. We aim at comparing the information gain, $\Phi(\pi_{(p=3,\lambda)}^A \| q)$, for the seven different scenarios previously introduced, i.e., when $A = \rho, D, H, (\rho, D), (\rho, H), (D, H)$, and (ρ, D, H) . The results below are obtained using $N = 10$ data points for each observable when taken individually, $N = 5$ for paired combinations, namely $A = (\rho, D)$, (ρ, H) , and (D, H) , and $N = 3$ in the last case, $A = (\rho, D, H)$.

Figure 3.10 shows $\Phi(\pi_{(p=3,\lambda)}^A \| q)$ computed for $\lambda = 0$, $\lambda = 0.25$, and $\lambda = 0.40$ as a function of the set, A , of observables chosen. The curves obtained for different values of λ are in close good agreement, consistent with earlier observations that lowering the tolerance does not significantly affect the results. As expected from the previous discussion, the largest information gain is obtained when the inference is run using all three observables, $A = (\rho, D, H)$. In addition, the behavior of the information gain for different combinations of observables can in fact be correlated with the corresponding behavior of the variances shown in Figures 3.8(b), (d), and (f). For brevity, the discussion of this analysis is omitted.

3.4. Comparison between deterministic and nondeterministic surrogates. We now provide a brief comparison of the inference results obtained using deterministic and nondeterministic surrogates.

Figure 3.11 shows the contour plots corresponding to 30%, 60%, and 90% of the maximum probability of the marginalized joint posteriors $\pi(\varepsilon, \sigma)$ (a), $\pi(\varepsilon, d)$ (c), and $\pi(\sigma, d)$ (e). The black line represents the results obtained using a third-order

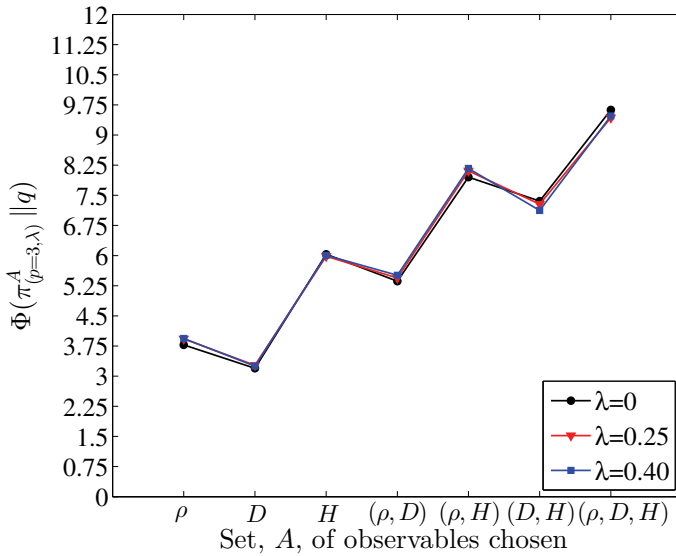


FIG. 3.10. *KL divergence $\Phi(\pi_{(p=3,\lambda)}^A \| q)$ from the prior, $q(\boldsymbol{\theta})$, to the posterior, $\pi_{(p=3,\lambda)}^A(\boldsymbol{\theta})$. The latter is obtained using a third-order nondeterministic surrogate model with $\lambda = 0$ (black), $\lambda = 0.25$ (red), and $\lambda = 0.40$ (blue). Color is more distinguishable in the online version. The set of observables, A , used in the inference is indicated on the horizontal axis.*

deterministic surrogate model, whereas the blue line represents those obtained using a third-order *nondeterministic* surrogate with $\lambda = 0$. The results are based on considering all three observables, (ρ, D, H) , with a total of 30 observations. For completeness, the right column shows the 3D plots of the KDE of the posteriors $\pi(\varepsilon, \sigma)$ (b), $\pi(\varepsilon, d)$ (d), and $\pi(\sigma, d)$ (f) color coded consistently with the figures on the left. The plots reveal that the posteriors obtained from a nondeterministic surrogate are exactly centered on the true values, whereas those obtained with a deterministic surrogate do not capture the true values with the same accuracy. For the present study, however, the results obtained from the two surrogates overall show small differences, also in the covariance structure. The blue and black contours plotted in the left column reveal, in fact, a similar orientation and a comparable spread. The 3D plots show a tight overlapping between the blue and black densities for all three cases presented, demonstrating that the differences are small but noticeable. Thus, in the present case the inference based on nondeterministic surrogates provides a more robust framework for performing the inverse problem.

To quantitatively evaluate the differences outlined above, we compute the KL divergence, $\Phi(\pi_{(p=3,\lambda,30)} \| \tilde{\pi}_{(\tilde{p},30)})$, from $\tilde{\pi}_{(\tilde{p},30)}$ to $\pi_{(p=3,\lambda,30)}(\boldsymbol{\theta})$. Here, $\tilde{\pi}_{(\tilde{p},30)}(\boldsymbol{\theta})$ denotes the marginalized joint posterior on the parameters, $\boldsymbol{\theta} = \{\varepsilon, \sigma, d\}$, obtained using a \tilde{p} th-order *deterministic* surrogate model for (ρ, D, H) and a total of 30 observations, i.e., $N = 10$, whereas $\pi_{(p=3,\lambda,30)}(\boldsymbol{\theta})$ is the marginalized joint posterior on the parameters obtained using a third-order ($p = 3$) *nondeterministic* surrogate model with a given λ , again using (ρ, D, H) and a total of 30 observations. The values of $\Phi(\pi_{(p=3,\lambda,30)} \| \tilde{\pi}_{(\tilde{p},30)})$ for different orders, \tilde{p} , of the *deterministic* surrogate and different values of λ are reported in Table 3.3.

The KL divergence $\Phi(\pi_{(p=3,\lambda,30)} \| \tilde{\pi}_{(\tilde{p},30)})$ decreases with increasing values of λ for $\tilde{p} = 2$. On the contrary, $\Phi(\pi_{(p=3,\lambda,30)} \| \tilde{\pi}_{(\tilde{p},30)})$ increases as λ increases from 0 to 0.40

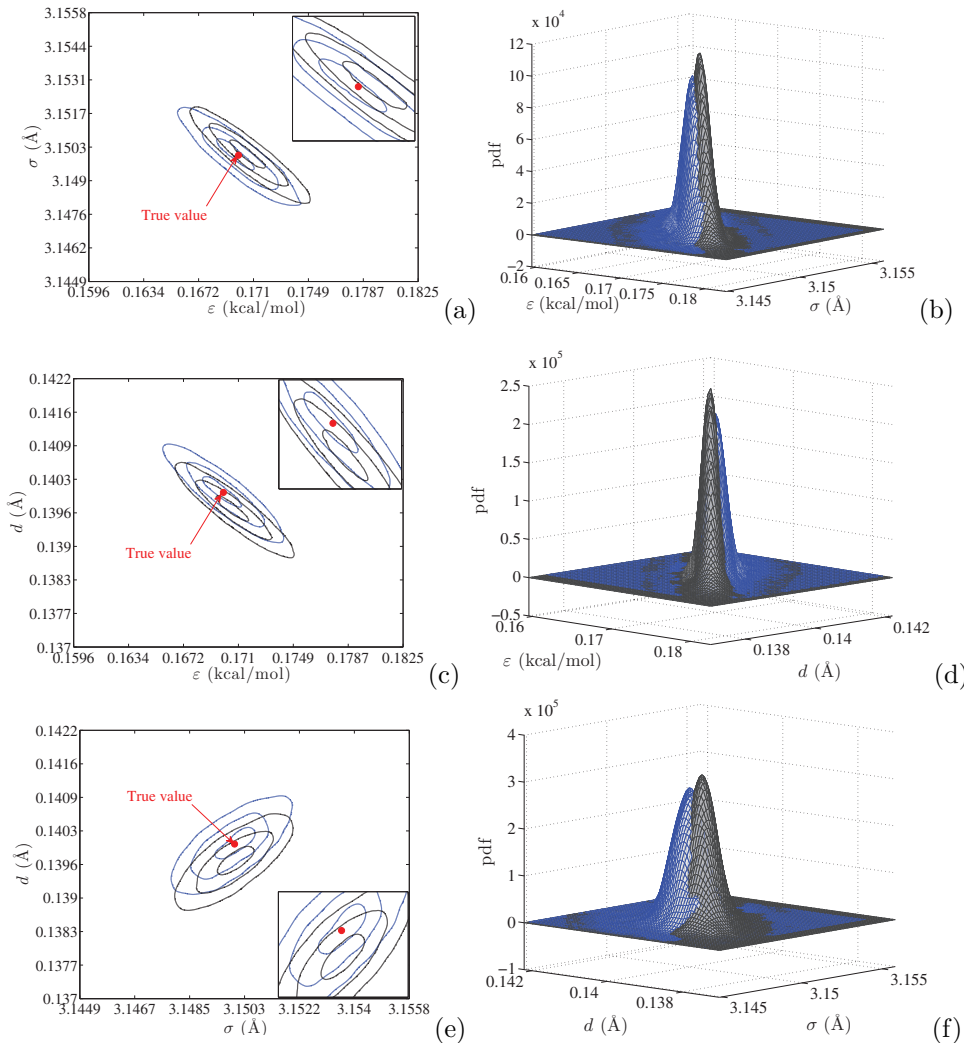


FIG. 3.11. Left column: contour plots corresponding to 30%, 60%, and 90% of the maximum probability of the marginalized joint posteriors $\pi(\varepsilon, \sigma)$ (a), $\pi(\varepsilon, d)$ (c), and $\pi(\sigma, d)$ (e). The black line represents the results obtained using a third-order deterministic surrogate model, whereas the blue line represents the results computed using a third-order nondeterministic PC surrogate with $\lambda = 0$. The results are based on considering all three observables, (ρ, D, H) , with a total of 30 data points. The right column shows the corresponding 3D plots of the KDE of $\pi(\varepsilon, \sigma)$ (b), $\pi(\varepsilon, d)$ (d), and $\pi(\sigma, d)$ (f) color coded consistently with the figures on the left.

for all the other cases, i.e., for $\tilde{p} \geq 3$. This result is due to the fact that as λ increases from 0 to 0.40, fewer sampling points are chosen at the third approximation level $l' = 3$ and, thus, the corresponding cubic *nondeterministic* PC surrogate tends to become increasingly closer to the quadratic expansion obtained at the second resolution level $l' = 2$ (see section 4.2 of Part I for details). Consequently, the differences between the results of the inverse problem run using a quadratic ($\tilde{p} = 2$) *deterministic* surrogate and those based on a cubic ($p = 3$) *nondeterministic* surrogate with a given value of λ diminish as λ increases from 0 to 0.40.

TABLE 3.3

Computed values of the KL divergence $\Phi(\pi_{(p=3,\lambda,30)}\|\tilde{\pi}_{(\tilde{p},30)})$ from the marginalized joint posterior on the parameters, $\tilde{\pi}_{(\tilde{p},30)}(\boldsymbol{\theta})$, obtained using a \tilde{p} th-order deterministic surrogate model, to the marginalized joint posterior, $\pi_{(p=3,\lambda,30)}(\boldsymbol{\theta})$, based on a third-order nondeterministic surrogate model with a given λ . The results are based on using all three observables, (ρ, D, H) , and a total of 30 observations, $N = 10$.

	$\tilde{p} = 2$	$\tilde{p} = 3$	$\tilde{p} = 4$	$\tilde{p} = 5$	$\tilde{p} = 6$
$\lambda = 0$	25.565	0.399	1.060	0.457	0.274
$\lambda = 0.25$	25.312	3.939	5.582	1.934	2.700
$\lambda = 0.40$	20.813	7.076	8.482	4.838	5.223

For $\tilde{p} \geq 3$, Table 3.3 reveals that, for a fixed λ , the value of $\Phi(\pi_{(p=3,\lambda,30)}\|\tilde{\pi}_{(\tilde{p},30)})$ varies little with \tilde{p} . Thus, the results obtained using a cubic *nondeterministic* surrogate for a given λ and those obtained using a \tilde{p} th-order *deterministic* surrogate are similar. This appears to result from the fact that, in the present case, the *nondeterministic* PC coefficients defining the surrogate expansions are characterized by a joint distribution with weak or nearly absent correlation and tightly centered around the corresponding MAP value (see section 4.2.2 of Part I for details). This is due to the fact that, in the present case, the MD sampling noise was relatively small [28]. If the MD sampling noise was very high, however, one might see a larger difference. The above analysis allows us to conclude that both the third-order *deterministic* and the *nondeterministic* surrogates are suitable for the inverse problem addressed in this work. The results, however, highlight the *nondeterministic* surrogate as the most suitable model to use in the context of noisy data.

3.5. Sensitivity of forward model predictions to parameter correlation.

Motivated by our earlier observations of a strong correlation structure between the inferred parameters, which was not part of our prior knowledge, we aim at exploring the effects of this correlation on the forward model predictions. The analysis is performed exploiting the posterior distribution $\pi_{(p=3,\lambda=0,30)}$, whose contour plots are depicted in Figure 3.11. Specifically, we use the corresponding statistics to create two different test distributions that share the same mean and marginal variance but differ in the correlation structure. One of these is designed such that it inherits the original correlation found for $\pi_{(p=3,\lambda=0,30)}$, while the other is constructed to have no correlation. The core of the analysis consists of sampling these two test distributions, exploiting these samples to obtain corresponding predictions for the observables of interest and, then, analyzing these predictions to capture the effects due to the correlation in the parameters.

The first test distribution is designed by fitting a *multivariate* Gaussian with mean, $\boldsymbol{\mu}$, and covariance matrix, $\boldsymbol{\Sigma}$, to the full *joint* posterior $\pi_{(p=3,\lambda=0,30)}$. This first test distribution can thus be written in short form as $\mathcal{N}(\boldsymbol{\mu}, \boldsymbol{\Sigma})$. We then generate samples of the parameters, $\boldsymbol{\theta}^{(i)}$, according to

$$(3.6) \quad \boldsymbol{\theta}^{(i)} \sim \mathcal{N}(\boldsymbol{\mu}, \boldsymbol{\Sigma}).$$

Figure 3.12(a) shows the 3D plot of $\{\boldsymbol{\theta}^{(i)}\}_{i=1}^{15000}$ generated according to (3.6). The results reveal the strong correlation structure between the parameters that is inherited from the original distribution.

For the second test distribution, we assume that no information about the correlation is available. We now generate samples of the parameters according to

$$(3.7) \quad \boldsymbol{\theta}^{(i)} \sim \mathcal{N}(\boldsymbol{\mu}, \text{diag}(\boldsymbol{\Sigma})),$$

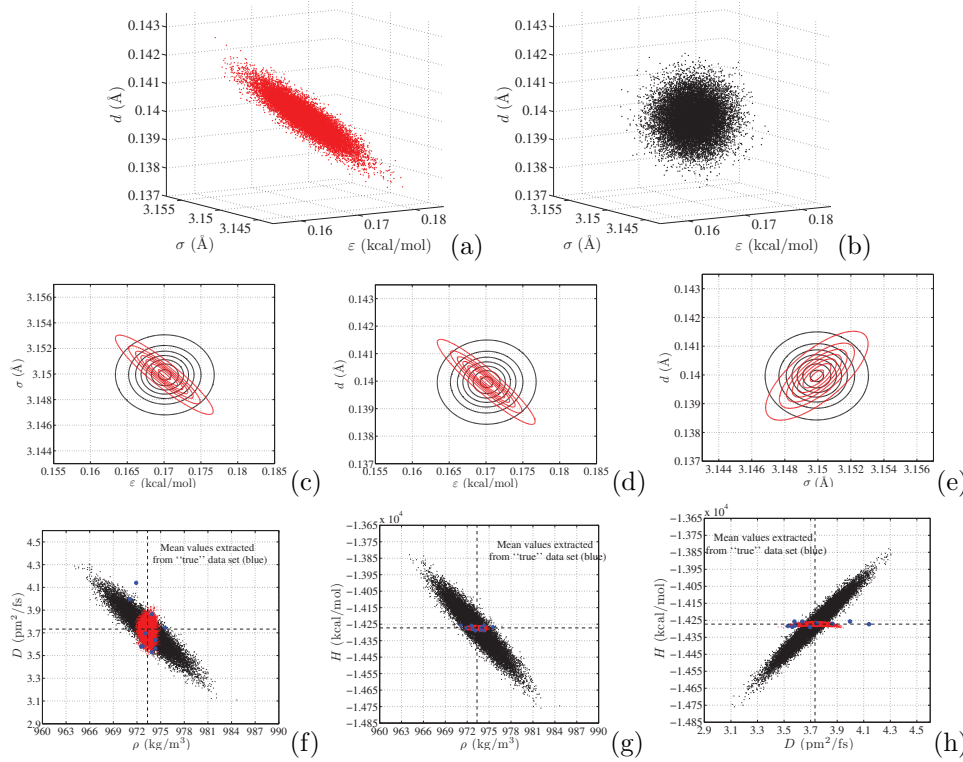


FIG. 3.12. Top row: 3D plot of 15000 parameter samples $\{\boldsymbol{\theta}^{(i)} = \{\varepsilon^{(i)}, \sigma^{(i)}, d^{(i)}\}\}_{i=1}^{15000}$ generated according to (3.6) (a) and (3.7) (b). Middle row: contour plots of the distribution of the samples for (ε, σ) (c), (ε, d) (d), and (σ, d) (e). The contours correspond to 0.05%, 0.2%, 0.35%, 0.5%, 0.65%, 0.8%, and 0.95% of the maximum probability. Bottom row: scatter plots of (ρ, D) (f), (ρ, H) (g), and (D, H) (h) obtained from surrogate evaluations using the parameters plotted above. The predictions obtained using the uncorrelated parameter samples are color coded black, whereas those from the correlated parameter samples are color coded red. Color coded blue are the original sets of 10 observations (Figure 2.2) of ρ , D , and H used to run the inverse problem, with their mean values represented with black dashed lines.

where $\text{diag}(\boldsymbol{\Sigma})$ represents the diagonal matrix obtained from the diagonal elements of $\boldsymbol{\Sigma}$. This case, therefore, neglects the off-diagonal elements of $\boldsymbol{\Sigma}$, making the parameters uncorrelated. Note, however, that the means and marginal variances of the parameters are equal to those in the case above. Figure 3.12(b) shows the 3D plot of $\{\boldsymbol{\theta}^{(i)}\}_{i=1}^{15000}$ generated according to (3.7). The samples show an isotropic distribution resembling a spherical shape, which results from the uncorrelation assumption.

To compare the sets of samples obtained from each case above, the second row of Figure 3.12 shows the contour plots of their projections on the (ε, σ) -plane (c), (ε, d) -plane (d), and (σ, d) -plane (e). The contours correspond to 0.05%, 0.2%, 0.35%, 0.5%, 0.65%, 0.8%, and 0.95% of the maximum probability. The contours are color coded consistently with the figures on the top. These plots clearly highlight the differences between the two sampling strategies considered, specifically with regard to the correlation, and reflect the constraint imposed that the means and marginal variances of the parameters remain equal.

The second step of the analysis involves using the sets of samples obtained above to generate corresponding predictions for density, self-diffusion, and enthalpy. Were

it feasible, one would use each of the 30000 samples of the parameters to run an MD simulation and extract corresponding predictions for ρ , D , and H . To make the problem computationally tractable, we consider an alternative strategy based on using the PC surrogate model to compute the predictions for the three observables of interest. Specifically, we employ a third-order *nondeterministic* expansion with $\lambda = 0$. This choice is somewhat arbitrary, but we verified the consistency of the results presented below also considering *deterministic* expansions of different orders. For brevity, however, these verifications are omitted.

The bottom row of Figure 3.12 shows the scatter plots of (ρ, D) (f), (ρ, H) (g), and (D, H) (h), based on 15000 data points obtained by evaluating the corresponding PC surrogate using the parameter samples plotted in panels (a) and (b). The predictions obtained using the uncorrelated samples of the force-field parameters are color coded black, while those obtained from the correlated samples are color coded red. The figures reveal that the correlation in the force-field parameters has a very strong effect on the predictions. In all cases, the uncorrelated parameter samples yield large correlations in the predicted observables. For the correlated parameter samples, however, the predictions are characterized by very weak correlations and their variances are substantially smaller than those of the correlated samples. Since the parameter samples are based on the posterior $\pi_{(p=3,\lambda=0,30)}$, one would expect the data to be consistent with the original observations. To assess this consistency, superimposed in Figures 3.12(f)–(h) and color coded blue are the original sets of 10 observations (Figure 2.2) of ρ , D , and H used to run the inverse problem, and we represent their mean values with black dashed lines. Figures 3.12(f)–(h) show, indeed, that all sets of predictions are nearly centered around the “true” means of the data. However, a major difference characterizes the variances of the predictions. The sets obtained from the *correlated* model parameters are very narrow, capture the means of the original “true” data with very good accuracy and small uncertainty, and are consistent overall with the “true” data. In contrast, the predictions obtained from the *uncorrelated* parameter samples yield larger spread in the data and substantially deviate from the “true” data.

4. Summary and conclusions. In this article, we explored the possibility of estimating a set of force-field parameters for TIP4P water using a Bayesian inference approach. We focused on a synthetic problem based on isothermal, isobaric MD simulations of TIP4P water at ambient conditions, $T = 298$ K and $P = 1$ atm. Presumed “true” values of the TIP4P parameters were used to generate a collection of noisy data of three macroscale observables: density, self-diffusion, and enthalpy. Following the work in [19], we leveraged the stochastic reformulation of the forward MD problem and the PC expansions of the macroscale observables derived in [28] to develop a reformulated Bayesian inference approach based on PC surrogate models.

We presented two separate formulations according to the nature of the PC expansions chosen as the surrogate model. In the first one, we adopted, as the surrogate model, the PC representations built using NISP. In this case, the PC expansions are *deterministic* since each expansion coefficient is identified by a single, well-defined value. We then illustrated an alternative strategy which exploited, as the surrogate model, the PC representations obtained using Bayesian inference. In this case, these PC models are *nondeterministic* since the coefficients are RVs with a specific joint probability density. For both approaches, we sampled the target posterior distributions using an AM algorithm, which yielded good results in terms of mixing and short burn-in periods for the chains. We discussed the results of the inverse problem based

on *deterministic* and *nondeterministic* surrogates individually, highlighting the main similarities and differences. We found that both approaches are suitable for the inverse problem addressed in this work, but the uncertain surrogate reveals a better performance, which would be even more evident in the context of noisier data.

We discussed the sensitivity of the inference on the type and number of observables used, showing that each parameter is very sensitive to certain observables, while being only minimally affected by others. The choice of observables used in the inference thus has a significant impact on the results. We showed that, in general, using a single observable leads to nearly uniform posterior densities, for which the information gain is minimal. When the number of observables considered increases, in most cases the information gain increases, and the corresponding posteriors accordingly become more informative. We demonstrated that, for a fixed number of observations, the variance in the inferred parameters can be drastically reduced only by modifying the set of observables considered. We explained this result by analyzing the structure of the PC surrogates, namely by generating parameter isosurfaces corresponding to the means of the inference data. The structure of these isosurfaces provided key insight into the dependence of the results on the choice of observables and demonstrated that the structure of the stochastic response surface plays a key role in determining the parameters' posteriors. We showed that the *nondeterministic* surrogate allows us to recover the “true” parameter vector with high accuracy using a third-order surrogate. We investigated the effect of the order of the surrogate model and found that, for the present case, higher-order surrogates did not yield significant improvement in the inference results.

Work is currently underway to extend the present work to address the problem of reparametrizing MD models based on macroscale experimental data. In this case, additional sources of uncertainty may arise, e.g., due to biases and correlations in the observations, and may consequently require a more elaborate framework.

REFERENCES

- [1] C. ANDRIEU AND E. MOULINES, *On the ergodicity properties of some adaptive MCMC algorithms*, Ann. Appl. Probab., 16 (2006), pp. 1462–1505.
- [2] Y. F. ATCHADÉ AND J. S. ROSENTHAL, *On adaptive Markov chain Monte Carlo algorithms*, Bernoulli, 11 (2005), pp. 815–828.
- [3] L. S. BASTOS AND A. O'HAGAN, *Diagnostics for Gaussian process emulators*, Technometrics, 51 (2009), pp. 425–438.
- [4] H. J. C. BERENDSEN, J. R. GRIGERA, AND T. P. STRAATSMA, *The missing term in effective pair potentials*, J. Phys. Chem., 91 (1987), pp. 6269–6271.
- [5] F. CAILLIEZ AND P. PERNOT, *Statistical approaches to forcefield calibration and prediction uncertainty in molecular simulation*, J. Chem. Phys., 134 (2011), 054124.
- [6] Y. EFENDIEV, T. HOU, AND W. LUO, *Preconditioning Markov chain Monte Carlo simulations using coarse-scale models*, SIAM J. Sci. Comput., 28 (2006), pp. 776–803.
- [7] R. GHANEM AND P. SPANOS, *Stochastic Finite Elements: A Spectral Approach*, Springer-Verlag, New York, 1991.
- [8] B. GUILLOT, *A reappraisal of what we have learnt during three decades of computer simulations on water*, J. Mol. Liq., 101 (2002), pp. 219–260.
- [9] H. HAARIO, E. SAKSMAN, AND J. TAMMINEN, *An adaptive Metropolis algorithm*, Bernoulli, 7 (2001), pp. 223–242.
- [10] H. W. HORN, W. C. SWOPE, AND J. W. PITERA, *Characterization of the TIP4P-Ew water model: Vapor pressure and boiling point*, J. Phys. Chem., 123 (2005), 194504.
- [11] H. W. HORN, W. C. SWOPE, J. W. PITERA, J. D. MADURA, T. J. DICK, G. L. HURA, AND T. H. GORDON, *Development of an improved four-site water model for biomolecular simulations: TIP4P-Ew*, J. Chem. Phys., 120 (2004), pp. 9665–9678.
- [12] W. L. JORGENSEN, J. CHANDRASEKHAR, J. D. MADURA, R. W. IMPEY, AND M. L. KLEIN,

- Comparison of simple potential functions for simulating liquid water*, J. Chem. Phys., 79 (1983), pp. 926–935.
- [13] W. L. JORGENSEN AND J. TIRADO-RIVES, *Potential energy functions for atomic-level simulations of water and organic and biomolecular systems*, Proc. Natl. Acad. Sci. USA, 102 (2005), pp. 6665–6670.
 - [14] A. G. KALINICHEV, *Molecular simulations of liquid and supercritical water: Thermodynamics, structure, and hydrogen bonding*, in Molecular Modeling Theory: Applications in the Geosciences, Rev. Mineralogy Geochem. 42, R. T. Cygan and J. D. Kubicki, eds., Geochemical Society, Washington, D.C., 2001, pp. 83–129.
 - [15] M. C. KENNEDY AND A. O'HAGAN, *Bayesian calibration of computer models*, J. R. Stat. Soc. Ser. B Stat. Methodol., 63 (2001), pp. 425–464.
 - [16] O. P. LE MAÎTRE AND O. M. KNIO, *Spectral Methods for Uncertainty Quantification*, Springer, New York, 2010.
 - [17] X. MA AND N. ZABARAS, *An efficient Bayesian inference approach to inverse problems based on an adaptive sparse grid collocation method*, Inverse Problems, 25 (2009), 035013.
 - [18] M. W. MAHONEY AND W. L. JORGENSEN, *A five-site model for liquid water and the reproduction of the density anomaly by rigid, nonpolarizable potential functions*, J. Chem. Phys., 112 (2000), pp. 8910–8922.
 - [19] Y. M. MARZOUK, H. N. NAJM, AND L. A. RAHN, *Stochastic spectral methods for efficient Bayesian solution of inverse problems*, J. Comput. Phys., 224 (2007), pp. 560–586.
 - [20] H. N. NAJM, B. J. DEBUSSCHERE, Y. M. MARZOUK, S. WIDMER, AND O. P. LE MAÎTRE, *Uncertainty quantification in chemical systems*, Internat. J. Numer. Methods Engrg., 80 (2009), pp. 789–814.
 - [21] J. OAKLEY AND A. O'HAGAN, *Bayesian inference for the uncertainty distribution of computer model outputs*, Biometrika, 89 (2002), pp. 769–784.
 - [22] J. OAKLEY AND A. O'HAGAN, *Probabilistic sensitivity analysis of complex models: A Bayesian approach*, J. R. Stat. Soc. Ser. B Stat. Methodol., 66 (2004), pp. 751–769.
 - [23] A. O'HAGAN, *Bayesian analysis of computer code outputs: A tutorial*, Reliab. Eng. Syst. Saf., 91 (2006), pp. 1290–1300.
 - [24] A. O'HAGAN AND J. F. C. KINGMAN, *Curve fitting and optimal design for prediction*, J. Roy. Statist. Soc. Ser. B, 40 (1978), pp. 1–42.
 - [25] C. E. RASMUSSEN AND C. K. I. WILLIAMS, *Gaussian Processes for Machine Learning*, MIT Press, Cambridge, MA, 2006.
 - [26] J. R. REIMERS, R. O. WATTS, AND M. L. KLEIN, *Intermolecular potential functions and the properties of water*, Chem. Phys., 64 (1982), pp. 95–114.
 - [27] F. RIZZI, *Uncertainty Quantification in Molecular Dynamics*, Ph.D. thesis, The Johns Hopkins University, Baltimore, MD, 2012.
 - [28] F. RIZZI, H. N. NAJM, B. J. DEBUSSCHERE, K. SARGSYAN, M. SALLOUM, H. ADALSTEINSSON, AND O. M. KNIO, *Uncertainty quantification in MD simulations. Part I: Forward propagation*, Multiscale Model. Simul., 10 (2012), pp. 1428–1459.
 - [29] G. O. ROBERTS AND J. S. ROSENTHAL, *Coupling and ergodicity of adaptive Markov chain Monte Carlo algorithms*, J. Appl. Probab., 44 (2007), pp. 458–475.
 - [30] G. O. ROBERTS AND J. S. ROSENTHAL, *Examples of adaptive MCMC*, J. Comput. Graph. Statist., 18 (2009), pp. 349–367.
 - [31] K. SARGSYAN, B. DEBUSSCHERE, H. N. NAJM, AND Y. MARZOUK, *Bayesian inference of spectral expansions for predictability assessment in stochastic reaction networks*, J. Comput. Theor. Nanosci., 6 (2009), pp. 2283–2297.
 - [32] D. S. SIVIA, *Data Analysis: A Bayesian Tutorial*, Oxford Sci. Publ., Oxford University Press, Oxford, UK, 2006.
 - [33] K. SZALEWICZ, C. LEFORESTIER, AND A. VAN DER AVOIRD, *Towards the complete understanding of water by a first-principles computational approach*, Chem. Phys. Lett., 482 (2009), pp. 1–14.
 - [34] C. VEGA, J. L. F. ABASCAL, M. M. CONDE, AND J. L. ARAGONES, *What ice can teach us about water interactions: A critical comparison of the performance of different water models*, Faraday Discuss., 141 (2009), pp. 251–276.
 - [35] A. WALLQVIST AND R. D. MOUNTAIN, *Molecular models of water: Derivation and description*, Rev. Comput. Chem., 13 (2007), pp. 183–247.
 - [36] J. WANG AND N. ZABARAS, *Using Bayesian statistics in the estimation of heat source in radiation*, Int. J. Heat Mass Tran., 48 (2005), pp. 15–29.
 - [37] N. WIENER, *The homogeneous chaos*, Amer. J. Math., 60 (1938), pp. 897–936.